

AperTO - Archivio Istituzionale Open Access dell'Università di Torino

Assessment of Density Functional Approximations for Highly Correlated Oxides: The Case of CeO₂ and Ce₂O₃

This is the author's manuscript

Original Citation:

Availability:

This version is available <http://hdl.handle.net/2318/1692588> since 2019-02-15T12:17:49Z

Published version:

DOI:10.1021/acs.jctc.8b00600

Terms of use:

Open Access

Anyone can freely access the full text of works made available as "Open Access". Works made available under a Creative Commons license can be used according to the terms and conditions of said license. Use of all other works requires consent of the right holder (author or publisher) if not exempted from copyright protection by the applicable law.

(Article begins on next page)

Assessment of density functional approximations for highly correlated oxides: the case of CeO₂ and Ce₂O₃.

Luca Brugnoli,¹ Anna Maria Ferrari,² Bartolomeo Civalleri,² Alfonso Pedone,^{1*} Maria Cristina Menziani.¹

¹*Dipartimento di Scienze Chimiche e Geologiche, Università di Modena e Reggio Emilia, Via G. Campi 183, I-41125 Modena, Italia.*

²*Dipartimento di Chimica, Università di Torino and NIS Centre of Excellence, Via P. Giuria 7, I-10129 Torino, Italia.*

Corresponding author:

alfonso.pedone@unimore.it

Abstract.

CeO₂ based materials are very attractive as catalytic component for industrial processes and environment friendly technologies, therefore, a reliable and computationally affordable theoretical description of the main properties of ceria is needed. In particular, the description of the interconversion between the Ce(IV) and Ce(III) oxidation states, on which lies the main chemical features of the Cerium Oxide, results quite challenging at the Density Functional Theory level. Here, we tested several Density functional approximations, spanning from GGA to Hybrid (Global, Meta-Global and Range Separated Corrected) functionals, on the structural, vibrational, electronic and thermochemical properties of bulk CeO₂ and Ce₂O₃. GGA and Meta-GGA xc best predict the thermochemical data, while the discrepancies increase with the introduction of the exact exchange in Hybrid functionals. Overall, the Short Range Corrected and Global Hybrid functionals with a percentage of Exact Exchange between 16 and 25 give the best description of the crystal properties. Then, a group of the best performing functionals has been tested on the formation energy of an oxygen vacancy at the (111) CeO₂ surface. In general, increasing the amount of exact exchange in the Hybrid functionals lead to a better description of the localized Ce 4*f* states, while the energy of formation of the O vacancy decrease, worsening compared to the experiment.

1. Introduction.

Conventional exchange-correlation (xc) functionals of the LDA and GGA families are the most used in solid state physics, where electronic structure codes based on plane waves basis sets are generally employed. However, these functionals present several shortcomings related to the lack of dispersion interaction terms and the well-known Self-Interaction Error (SIE)¹. The inability of standard xc functionals to describe long-range electron correlations causes serious difficulties in simulating the structure and properties of systems where van der Waals forces are dominating, and in the correct determination of the energy stabilities of transition metal oxides². Instead, the latter deficiency negatively affects the simulation of the geometry and electronic structure (band gaps), defect formation energies, spin localization, magnetic and thermodynamic properties of highly correlated systems; that is, those containing d and f electrons.

In this context, methods based on the addition of C_6/R^6 empirical dispersion terms and correction for on-site Coulomb correlation effects by a Hubbard-type U term (DFT+ U) have been proposed and usually applied in order to maintain affordable computational costs. The choice of the U value in the DFT+ U approach is not straightforward since it must be large enough to correctly localize highly correlated d and f electrons (depending on the system under study), without introducing artefacts such as overestimated band-gaps. Moreover, it has been shown that in most cases it might be necessary to employ different U values for different properties or systems under study³.

Alternative approaches consist in using hybrid functionals (where a fraction of the HF exchange is added to the GGA-DFT exchange energy) or the Range Separated Hybrids (RSH) functionals (where the $1/r$ operators in the exact exchange (EE) term is partitioned in different regions based on inter-electronic distance). However, whereas some hybrid functionals have been implemented in plane-wave (PW) DFT based codes (albeit they are very computationally demanding) they have been considered impractical for crystalline solids, at least for Global Hybrids and Long Range Separated Hybrids⁴. On the contrary, approaches based on atom-centered basis functions (as for Gaussian Type Orbital (GTO)) permit an easier and efficient implementation; for instance several functionals belonging to all families (LDA, GGA, Meta-GGA, GH and RSH) have been recently implemented in the CRYSTAL code.⁵

Since most of the Meta-GGA, GH and RSH functionals have been designed and optimized for molecular systems, it is interesting to assess their performances in predicting the structure and properties of highly correlated solid systems.

Here, we have considered cerium oxides, either stoichiometric CeO_2 , non-stoichiometric CeO_{2-x} , and the antiferromagnetic sesquioxide Ce_2O_3 . These are important systems for several industrial applications, in fact ceria is traditionally used as support material in components of three-way

catalysts in automotive catalytic converters, fluid-cracking catalysts in refineries, fuel-cell electrodes and low-temperature CO and VOC oxidation catalyst, hydrocarbon reforming, water-shift reaction etc...⁶.

The broad use of ceria in heterogeneous catalysis is due to the easy conversion between the two-oxidation states $Ce^{4+} \leftrightarrow Ce^{3+}$. The simulation of stoichiometric ceria (with all Ce^{4+} ions) is not problematic with the conventional *xc* functionals since the *4f* orbitals are empty. The problem arises for systems (defective bulk and surface ceria) containing Ce^{3+} ions, which have partially occupied atom-like localized *4f* orbitals. In fact, in the case of the formation of an oxygen vacancy the SIE, which tends to over-delocalize the electrons, prevents the localization of the excess of spin density in the *4f* cerium orbitals with integer occupation numbers. Moreover, the SIE also leads to the underestimation of energy barriers for surface chemical reactions⁷ and the underestimation of band gaps leading sometimes to metallization⁸.

Because of its large use in industry cerium oxides have been widely theoretically investigated in the past. Most of these studies were carried out using the cost-effective DFT+U approach^{3,9-13} and the main results relative to the oxygen defects and surface chemistry of Ceria have been reviewed in ref.¹⁴ The electronic structure of CeO_2 and Ce_2O_3 was first investigated by using meta-GGA (TPSS) and screened (HSE) hybrid functionals in conjunction with the Gaussian orbitals basis set by Hay et al¹⁵ whereas periodic plane-wave DFT calculations using the PBE0 and the HSE hybrid functionals were carried out for the first time by Da Silva et al.⁹ They found that hybrid functionals correctly predict the antiferromagnetic form of Ce_2O_3 and the structural properties of the two oxides, whereas the band gaps were overestimated by 45% and 15% by PBE0 and HSE, respectively.

The first B3LYP¹⁶ calculations on cerium oxides were performed by Kullgren et al.¹⁷ who found that B3LYP performs slightly better than PBE0 for the electronic properties but slightly worse for the structural ones.

Subsequently, Graciani et al.¹⁸ examined the performance of the HH, HLYP¹⁹PBE0²⁰, B3LYP¹⁶ and the B1WC²¹ hybrid functionals on the reproduction of bulk properties (structure and band-gaps) and the reaction energies for reduction of CeO_2 to Ce_2O_3 releasing O_2 . All the functionals gave good cell parameters and overestimated *2p-4f-5d* (CeO_2) and *4f-5d* (Ce_2O_3) band gaps that decrease with the drop of the exact exchange contribution in the *xc* functional. Instead, the reduction energies were underestimated. The B1WC functional was proposed as the one that best reproduces the aforementioned properties. Finally, surface properties and the oxygen vacancy formation energies in CeO_2 were accurately described with the PBE0 functional and GTO basis sets by Désaunay et al.²² and Evarestov et al²³., respectively.

Finally, very recently Spin localization, magnetic ordering, and electronic properties of strongly correlated Ln_2O_3 sesquioxides ($\text{Ln}=\text{La}, \text{Ce}, \text{Pr}, \text{Nd}$) have been investigated by using global hybrids and GTOs including g functions.

In this work, we report an extensive comparative study of the performance of 27 functionals belonging to the different Rungs of the Jacob's Ladder namely GGA, Meta-GGA and Hybrid functionals (Hyper GGA), both Global and Range Separated Hybrids.

We preliminary have compared the accuracy of the combination of three basis set for Ce (Ce1, Ce2, Ce3) and two for O (O1, O2), from the less extensive combination Ce1/O1 to the larger one Ce3/O2 using the PBE0 functional on the reproduction of the bulk properties (cell parameters, bulk modulus, elastic constant and band gaps) and the thermochemistry of reduction of the two cerium oxides. Then, chosen the smallest effective basis set, we have tested all the aforementioned functionals on the reproduction of the same bulk properties. Finally, the most promising functionals have been used to investigate the relative stabilities and the spin localization of oxygen vacancies at the (111) ceria surface.

2. Computational Details

All the calculations were performed with the package CRYSTAL14⁵ at exception of the calculations that made use of the CAM-B3LYP functional for which the CRYSTAL17 version was used.²⁴

A total of 27 different flavours of exchange correlation functionals were used: 1 GGA (PBE²⁵), 1 Meta-GGA (M06-L²⁶), 5 Meta-GHs (M05²⁷, M05-2x²⁸, M06²⁹, M06-2x²⁹, M06HF²⁶), 9 global hybrids (B3LYP¹⁶, B3PW^{16,30}, PBE0²⁰, PBE0-13³¹, PBEsol³², PW1PW91³³, WC1LYP³⁴, B97H^{35,36}, B1WC²¹) and 10 RSH (HSE06^{25,37}, HSEsol^{32,38}, HISS^{25,39,40}, LC- ω PBE^{25,41}, LC- ω PBEsol^{32,41}, LC- ω BLYP⁴², RSHXLDA^{43,44}, ω B97^{35,45}, ω B97-X^{35,45}, CAM-B3LYP²⁴) functionals. (See table S1 of the ESI for an overview of the main characteristics of the xc functionals employed).

To compare the results of Hybrid functionals with a method not suffering from SIE we have also performed calculations within the Hartree-Fock framework.

Cerium was described using a relativistic small core Effective Core Potential (ECP) developed by Dolg and co-workers⁴⁶ which replaces the $1s^2 2s^2 2p^6 3s^2 3p^6 3d^{10}$ inner core, while the remaining $4s^2 4p^6 4d^{10} 5s^2 5p^6 4f^1 6s^2 5d^1$ electrons were treated as valence.

This ECP was the same used in previous works^{13,15,16,20} and it has been showed to be the most suitable to describe both CeO_2 and Ce_2O_3 . Then, three valence basis sets were employed to describe the Ce valence electrons: the one used by Graciani et al.¹⁸ (named Ce1, hereafter), a modification of this with an added contraction constituted of a single Gaussian primitive with exponent 0.27 for the $5d$ shell (named Ce2, hereafter) and finally, a pruned version of the segmented basis set developed by Dolg and co-workers⁴⁷. In the latter case, we removed all g functions, not supported by CRYSTAL14, and

all the functions with exponents lower than 0.11, to avoid pseudolinear dependency issues. The resulting basis was named as Ce3.

For Oxygen we used the same basis set employed by Graciani et al¹⁸ (named O1, hereafter) and a larger basis set of Quadruple-Zeta plus polarization quality⁴⁸(O2). For Hydrogen a Triple-Zeta plus polarization BS was used⁴⁹. All the BSs have been reported in the ESI.

To check the effect of the BS on the properties of the two oxides, the 6 combinations of the aforementioned BSs of different sizes were tested with the PBE0 functional.

To reduce the computational burden we investigated only the ferromagnetic state for Ce₂O₃ instead of the ground state antiferromagnetic, which requires a broken symmetry or a supercell approach. This decision is supported by the extremely low difference in energy of the two states, found by previous works and demonstrated by the extremely low Neel temperature⁵⁰ (proof of a very weak magnetic coupling). To accelerate the SCF (Self Consistent Field) convergence of the Ce₂O₃ the initial occupation of 4f AOs of Ce have been set using the keyword FDOCCUP to have a ground state formed by a mixing of the components $(2z^2-3x^2-3y^2)z$ and $(x^2-3y^2)x$.

The reciprocal space of the primitive lattices of both oxides was sampled with a Monkhorst-Pack grid 6 x 6 x 6 for all the calculations with the hybrid functionals, except for the computation of the elastic properties, which required the use of a finer k-point mesh of 12 x 12 x 12. The radial and angular point for the integration grid were generated according to the Gauss-Legendre radial quadrature and Lebedev two-dimensional angular point distribution schemes. The default grid (XLGRID) was employed for all calculations. The truncation criteria of the Coulomb and exchange infinite lattice series are controlled by five thresholds (T1,T2,T3,T4 and T5), which have been set to 8 (T1–T4) and 20 (T5) for all the calculations.

Default convergence thresholds on gradients and displacements were used for all the geometry optimizations of the primitive cells of CeO₂ and Ce₂O₃, while the threshold on energy change was raised to 10⁻⁸ Hartree for the geometry optimization and elastic properties computations and to 10⁻¹⁰ Hartree for frequencies calculations at the Γ point. Both the atomic positions and the lattice parameters were optimized for the primitive structures until the full convergence of atomic gradients and displacements.

Elastic properties were calculated according to the model of Reuss-Voigh-Hill for polycrystalline materials, following the automated procedure implemented in the code^{51,52}.

Defects calculations. Oxygen vacancies were modelled on the surface (111) of CeO₂, employing a 2D slab model with a p(2x2) periodicity of the surface unit cell, composed by 3 CeO₂ layers (overall 36 atoms for the pristine cell). This is the same model employed by Ganduglia-Pirovano et al⁵³ in their HSE06 and DFT+U investigation on the stability of the configurations of the O vacancy and it

is justified by the experimentally observed ordering of oxygen vacancy after annealing of a surface 111 of CeO_2 ⁵⁴. The model does not simulate the isolated vacancy, the defect concentration is $\theta=1/4$, but it is considered sufficiently accurate to allow a consistent comparison of the results with different xc functionals.

In our approach, we remove the O atom but leaving the basis set of Oxygen as ghost functions to describe the electron density of the vacancy.

The reciprocal space for the periodic 2D slab model were sampled with a k-point mesh of 4 x 4 x 1 for the structure optimization, employing the basis set Ce2/O1.

We investigated only the ferromagnetic ordering of the Ce^{3+} since most authors reported extremely low magnetic coupling.

The total energy was then computed from single point calculations on the optimized structures employing the largest basis set combination Ce3/O2, with a k-point mesh of 6 x 6 x 1.

In all these calculations, the lattice constants were fixed to the bulk optimized values while the atomic positions in the cell were free to relax. The starting guess for the occupation matrix was made by the atomic configuration of Ce and O, without assigning an initial spin polarization to the single atoms. With this relaxation scheme the excess of spin density localize on two Ce nearest neighbours (nn_nn configuration) to the vacancy, with all the hybrid xc tested.

The structures were considered optimized when the maximum atomic gradient was below 0.00045 Hartree/Bohr and the energy change from subsequent steps was below 10^{-6} Hartree.

3. Result and discussion

Before undertaking the extensive benchmarking of functionals for the prediction of the cerium oxides's properties we tested different BSs using the PBE0 functional.

The results obtained for the lattice parameters, elastic constants, energy reduction, band gaps and vibrational frequencies computed for both oxides are reported in Tables S2 and S3 and discussed in the section 3 of the ESI.

The largest BS (Ce3/O2) provides higher accuracy with respect to the experimental data for most of the properties investigated. Moreover, overall the modified basis Ce2/O1 performs better than the original one for all the properties tested, the results being similar to those obtained with the largest BS used (Ce3/O2).

Therefore, in the following all the calculations on CeO_2 , Ce_2O_3 , and defective CeO_2 are performed with the basis Ce2/O1, with the exception of the energy of reduction and of formation of the O vacancies for which the largest BS Ce3/O2 has been used.

3.1 Structural and elastic properties.

Ceria. CeO₂ crystallizes in the fluorite structure and belong to the same space group $\overline{\text{Fm}}\ 3\ \text{m}$, with an experimental lattice constant value for the crystallographic cell of 5.411 Å at room temperature⁵⁵ and a 0 K extrapolated value of 5.391 Å⁵⁶, which would be the best reference for static DFT calculations.

The cell parameters computed with the tested functionals are reported in Table 1. All functionals reproduce well the lattice parameter, with the largest deviation (about 0.1 Å) computed by the Meta-GGA M06L functional. The smallest deviations are provided by hybrid functionals based on the PBE exchange correlation, while the ones with the LYP correlation slightly overestimate the lattice parameter. The same behaviour was also reported for other systems by Paier et al⁵⁷ and it was attributed to the failure of the LYP correlation in reproducing the energy of the homogenous gas limit. In fact, the B3PW functional, in which the correlation term is formed by the PWGGA correlation, performs similarly to PBE0, and gives results close to experiment, as well as PW1PW91.

PBE0 and HSE06 give results very similar and close to experimental values, while the related xc for solids PBEsol0 and HSEsol give slightly smaller cell parameters.

The results obtained with PBE, PBE0 and B3LYP are closer to experiment data than the ones reported by Désaunay et al²² and in agreement with those reported by Kullgren et al¹⁷ using GTO BSs.

The PBE, PBE0 and PBE0-13 results show that increasing the fraction of Exact Exchange (0, 0.25 and 0.33, respectively) shorten the lattice parameter, confirming the results by Graciani et al¹⁸.

Regarding the Minnesota family of hybrid functionals, M06, M06-2x and M05-2x seem to provide the best results.

The adiabatic bulk modulus computed with all the functionals are also reported in Table 1, as well the independent elastic tensor components. The bulk modulus is significantly sensitive to the equilibrium structure from which it is calculated, and thus small deviations in the lattice constants lead to significant variations in the elastic tensor components: the smaller lattice parameter the larger bulk modulus, and vice versa. Figure 1 shows the trend observed for the different families of functionals, with Meta Global Hybrids (M-GHs) and Long Range Separated-Hybrid (LRHs) providing more rigid structures compared to Short Range and Global Hybrids (SRHs and GHs). The M-GHs shown higher slope than the others.

HF calculations predict a higher bulk modulus compared to the xc functionals that predict similar reticular lattice, probably due to the higher ionic character yielded by this method. To this regard, we find for the series PBE, PBE0, PBE0-13 a direct proportionality between the Mulliken's charge of Ce (2.35, 2.59, 2.66 respectively) and the bulk modulus (176.9, 212.6, 222.7 GPa).

M-GHs incorporating a high fraction of EE (above 50 %), as M05-2x, M06-2x, and M06HF, better reproduce the lattice parameter compared to the M06 and M05, but the computed bulk modulus is higher than the one obtained from GHs with a similar lattice constant. The high amount of exact exchange is not sufficient to explain the higher rigidity obtained by the Minnesota family of functionals. A possible explanation for this behaviour is the inclusion of the description of the dispersion forces by the Minnesota family of functional resulting in stronger cohesive forces. Overall, the smallest deviation from the experimental adiabatic bulk modulus and the elastic tensor components has been obtained with HSE06 and the GHs family, the largest with the Minnesota M-GHs family.

Ce_2O_3 . Cerium sesquioxide (phase A) belongs to the hexagonal spatial group $P\bar{3}m1$, with a ratio between the lattice vectors c/a of 1.56. The experimental room temperature values for a and c are 3.891 Å and 6.059 Å⁸¹, respectively. The structure has been optimized without constraints on the lattice parameter ratio. As anticipated in the computational section the ferromagnetic ground state of Ce_2O_3 has been investigated instead of the antiferromagnetic one, although the latter is slightly lower in energy, due to the higher computational cost of the latter. The results, reported in Table 2, show that the lattice parameter a of the hexagonal base is little affected by the different xc approximations; a smaller dispersion of the values compared to the c parameter is highlighted. The same behaviours observed for the structural features of CeO_2 is found for Ce_2O_3 : PBEsol based functionals show overbinding with respect to the PBE based ones, while LYP correlation overestimate the c lattice vector more than a , leading to an elongation of the cell along the z axis.

Table 2 reports the Hill values for the adiabatic bulk modulus, calculated as average of the Voigt and Reuss bulk modulus, which have been obtained from the computed elastic constants. To the best of our knowledge, there are no other hybrid DFT studies of the elastic properties of the Ce_2O_3 crystal in the literature and only one experimental data of the bulk modulus has been found to be 111 GPa⁵⁸. All the functionals used overestimate the experimental bulk modulus (of about 10-45 GPa) at exception of the PBE one that provides a very good agreement (109 vs 111 GPa) and M06L functional which overestimates it by 10 GPa. All the Hybrids that reproduce accurately the lattice structure overestimate the bulk modulus of at the least 25 GPa, while smaller deviations are observed for the xc predicting structures with larger volumes. However, given the dispersion on the experimental data reported in the literature most of the results can be considered acceptable.

3.2 Cohesive energies

Table 3 compares the computed cohesive energies (referred to the primitive unit cells) for both oxides with the experimental values. The formers have been obtained by subtracting to the total electronic energy of the solid the atomic energy of O and Ce, both calculated in the triplet states. For computing atomic Ce, the basis Ce3 has been augmented including all the diffused primitives of symmetry s, p and d of the original basis set. The atomic energies have been calculated with Crystal14 for all the functionals, and checked with Gaussian09⁵⁹ for few functionals (PBE0, M06L, PBE, B3LYP, HF): the differences are all below 0.01 eV. The inclusion of g functions to the Ce basis set (Gaussian09) decreases the atomic energy of about 0.02 eV, which is negligible to the purpose of the benchmark. The latter have been obtained by subtracting to the tabulated standard enthalpy of formation of the solid, the enthalpy of atomization of α -Ce (most stable phase) and of dissociation of O₂.

The deviation of the calculated values with respect to the tabulated ones are reported in Figure 2 for both CeO₂ and Ce₂O₃. Very small deviations for both solids are obtained by using M06L, PBE, B1WC, HSEsol and PBEsol0 functionals.

3.3 Electronic Structure.

Ceria. Several experimental studies have investigated the electronic structure of CeO₂ to characterize the band gaps without providing definitive results, since the lack of accurate experimental band gaps makes the assessment of the theoretical methods difficult.³ However, as shown in Figure S1 of the ESI, the conduction band (CB) of CeO₂ is constituted by Ce 5*d* like states, while the upper valence (VB) is well described as O 2*p* filled states, and between them there are the empty Ce 4*f* states.

The reported experimental range of values spawns the interval 2.6-3.9 eV for the O 2*p* - Ce 4*f* gap and 5.5-8 eV for the fundamental O 2*p* - Ce 5*d* gap, but many previous theoretical investigations took as reference value 3 and 6 eV for the two gaps, respectively. For the sake of simplicity, we report in Figure 3 the difference between the calculated gaps and the experimental values of 3 and 6 eV, being aware that the experimental uncertainty is large. The full set of numerical data are reported in Table S4 of the ESI.

All the LRHs largely overestimate the band gaps, showing that a high amount of EE at long range is not suitable to describe accurately the electronic structure, as has been reported by Pernot et al⁶⁰. Instead, HISS, which use only 60% of exact exchange at medium range, predicts a gap barely over the upper limit, similar to PBE0 with the 25% of EE at full range. HSE06 gives an appropriate description of the electronic structure of CeO₂, in agreement with previous work²³, as well as HSEsol. PBE0 and PBEsol0 overestimate the gaps. The Minnesota functionals give results highly dependent on the amount of exact exchange: M06L, which does not incorporate the exact exchange, predicts a small band gap, slightly over the one computed with PBE. M05 and M06, with respectively 28 and

27 % of full range exact exchange, reach the upper limit of the interval. M05-2x and M06-2x, in which the exact exchange is doubled compared to the original formulations, overestimate it. M06HF, with 100% of exact exchange in the full range severely overestimate the band gap, giving results very similar to the Hartree-Fock ones. With both M06HF and HF the Ce 4*f* and the Ce 5*d* empty bands results almost merged, with virtually no gap among them, while for all the other functionals the 2 virtual bands are separated by about 2.5-3.5 eV. All the Density of States for CeO₂ and Ce₂O₃ are reported in the ESI, section 7 and 8, respectively.

Xc functionals able to reproduce the O 2*p* - Ce 4*f* gap within the experimental interval are global hybrids that employ a fraction of exact exchange between 0.16 and 0.21 (B1-WC, WC1LYP, PWPW91, B3PW and B3LYP) and the Short Range corrected HSE06 and HSEsol.

The gap O 2*p* – Ce 5*d* is overestimated by most hybrids functionals, the only results close to the lower limit are the one from PBE and M06L. Interesting, for GHs a steeper linear dependence of the band gaps by the amount of EE is observed compared to M-GHs.

Ce₂O₃. The band gaps of Ce₂O₃ computed with all the tested functionals are compared with the experimental ones in Figure 4 and Table S5. The reported experimental gap for Ce₂O₃, which involve the valence formed by the localized Ce 4*f* states and the conduction constituted by a mixture of Ce 4*f* and Ce 5*d* states is an optical gap: it should be a lower bound to the fundamental gap, which instead is better reproduced by the hybrid functionals⁶¹. Once again, the lack of an accurate reference for the experimental band gap⁶² makes the assessment of the functionals rather difficult. Similarly, to the CeO₂ case, the gap is largely overestimate by all the LRHs and M-GHs and most GHs. The best performers are, as for CeO₂, the SRHs HSE06 and HSEsol, together with B1WC, PW1PW91, WC1LYP. M06L, which predict a gap of 0.6 eV, performs similarly to TPPS, predicting a small band gap compared to the metallic solution of the GGA PBE, but still 1.8 eV below the experimental value. Recently, Tran and Blaha⁶³ have investigated the performance of many functionals, including hybrids and Meta-GGAs, on the band gap for several solids: the Meta-GGA mBJLDA⁶⁴ has obtained the best results outperforming B3PW91 and HSE06, that are known to be among the best performers for semiconductors. They, as many others before, studied small, medium and large gap solids, including many correlated transition metal oxides, except cerium oxides and other highly correlated *f* electrons compounds.

Table S5 shows an inverse dependence of the Ce 4*f* – O 2*p* intragap with the amount of EE. This relation is more evident for the GHs and M-GHs were the exact exchange is computed in the full range. A larger amount of EE widens the band gap by increasing the energy of the virtual band and decreasing the energy of the occupied levels but affecting more the states closer to the Fermi level: the occupied Ce 4*f* states are downshifted more than the O 2*p* states, reducing the energetic difference.

M06HF with 100% in the full range, reduce the gap to zero, leading to an overlap of the two occupied bands and providing the same picture obtained with the non-correlated Hartree-Fock. This odd behaviour is similar to the one observed with DFT + U for higher values of U⁶⁵, and it has been attributed to the non-orthogonality of the O 2*p* and Ce 4*f* states⁶⁶.

3.4 Vibrational Properties.

Ceria. The harmonic frequencies have been computed at the Γ point exploiting the full symmetry of the lattice space group. Results obtained for PBE0 show that the computed frequencies are significantly affected by the basis set quality, approximating the experimental values as the basis set increase. For PBE0/Ce2O1, the basis set effect leads to a blue shift of 21 cm⁻¹ for the IR active bending (F_{1u}) and of 7 cm⁻¹ for Raman active stretching (F_{2g}) of CeO₂. The results can be used as references to evaluate the best functional for furthermore accurate investigations of phonon dispersion and thermodynamic functions. All the calculated frequencies are reported in the Table 4.

The difference between the calculated Harmonic frequencies and the experimental ones for the two modes (F_{1u} and F_{2g}) are reported in Figure 5. The best agreement with the experiment is observed for HSE06 and GHs (which better approximate the lattice parameter and the bulk modulus), with the exception of B97H. The PBE0 frequencies computed with the basis Ce3/O2 are similar to the HSE06 ones. The results obtained with HSE06 are in good agreement with recent work⁶⁷, where the vibrational properties of CeO₂ and Ce₂O₃, other than pristine and defective CeO₂ surfaces, were compute with HSE06 and PBE+U.

Overall, the functionals that predict lattice structures with good accuracy should also reproduce the frequencies reasonable well, as overbinding leads to higher frequencies and underbinding leads to lower ones, but we have observed in the previous sections that M-GHs, as well as LRHs, overestimate the rigidity of the structure, predicting higher frequency with the same lattice parameters.

Ce₂O₃. Only the Raman Spectrum has been recently recorded for the hexagonal phase of Ce₂O₃⁶⁸, and very partial data of the IR spectrum exist. Table 4 lists all the computed stretching and bending modes Raman and IR active. We selected three of the best performing GHs to simulate the Raman spectra employing the largest basis set combination Ce2/O3. Figure 6 reports the simulated Raman Spectra for the selected xc, superimposed on the experimental spectra (anti-Stokes Raman scattering) from Ref 68. Even if the intensities are not perfectly reproduced, the best agreement is obtained with PBE0.

3.5 Thermochemistry of reduction

In order to assess how different functionals are able to reproduce the energetics of reactions involving the CeO₂ and Ce₂O₃ oxides the following reduction reactions have been considered:



As stated by Paier et al¹⁴, Zero-Point vibrational energies and thermal contributions are small for the enthalpies of formation of the two oxides⁶⁹, as well for the reactions involved, so that these enthalpies can be compared to the DFT energies at 0 K without further corrections. As mentioned before, the reduction energy is an important descriptor of the energy of formation of the oxygen vacancy in the metal oxide. Therefore, a method able to reproduce the reduction energy is expected to give also a good description of the oxygen vacancy formation, provided that the correct nature of the vacancy is reproduced⁷⁰.

PBE gives a good approximation of the reduction energy, but it doesn't reproduce correctly the enthalpy of formation of CeO₂ and Ce₂O₃, neither the 4*f* localized states of the O vacancy¹⁴.

To calculate the enthalpy of the reaction 1 (R1) it is necessary to calculate the electronic energy of O₂ and O, both in the triplet state. Graciani's BS O1 gives bonding energy that are on average 0.9 eV lower than the one computed with our highest quality basis BS O2 (see Table S6).

This is because Graciani's BS is a small one optimized to minimize the energy of CeO₂, but it has not been optimized to well describe molecular O₂. Larger basis set usually do not need to be re-optimized since the high number of primitives in the BS should ensure enough variational freedom. However, to avoid convergence problems in solid state periodic calculations it is often required to remove or adjust too diffused primitive functions, at the cost of losing applicability to molecular systems.

The Reaction 2 (R2) avoids the general problem of the DFT methods in describing open shell systems, which for our case can lead to large errors in the prediction of the strength of the O-O bond. However, as can be seen in Figure 7, the results shown that both reactions provide similar deviations from the tabulated enthalpies. The corresponding numerical values are reported in Table S7 of the ESI.

After PBE, M06L gives the better performance for both reactions, and differently from PBE it also reproduces the experimental bonding energy of O₂. This result is interesting in view of the fact that this M-GGA has been developed and parameterized to study reactions involving transition metals. However, as observed previously, its performance is poor concerning many other properties of interest.

All the hybrid functionals investigated underestimate the reduction energies of both reactions 1 and 2, with an average error of 1.88 eV and 1.97 eV with respect to the tabulated experimental data. GHs give the smallest average deviations, as well the SRHs, while the Long Range Corrected ones underestimate both reaction enthalpy by 2 eV or more. The Minnesota family of M-GHs is the worst performer, apart from M06, which predicts energies comparable to the ones of GHs.

Previously, Graciani et al¹⁸ found an inverse relation between the amount of EE and the reduction energy of CeO₂ to Ce₂O₃ for the xc PBE0, B1WC and B3LYP. The results obtained here with the several xc functional confirm this finding: the highest energies of reduction, which are more similar to the experimental ones, are obtained with PBE and M06L (0% EE) followed by B1-WC and WC1LYP (16% EE). Within the GH family, which cover the range 16-33% of EE, the highest and smallest energies are found for the two extremes, respectively. Indeed, in the interval 20-25% the effect of the HF like exchange is covered mainly by the effect of the local part of the xc. For the LRHs, the high fraction of exact exchange at long range heavily reduce the reduction energies; the smallest deviation from experiment is obtained by CAM-B3LYP, with 90% EE at long range against 100% of all the others. Among the Minnesota M-GHs, M06, with 27% EE produces results similar to GHs with 20-25% EE, while M05 with 28% EE gives much worsen results. M06-2x, with 54% EE gives the largest deviation from the experimental results.

To explain these results, we have considered the effect of the EE on the filled bands of the solid: the intra-gap of O 2*p* – Ce 4*f* in Ce₂O₃ decreases as the weight of the exact exchange increases. The reaction of reduction involves the extraction of a neutral O atom, which leave in the solid two unbound electrons, which occupy the 4*f* states of Ce. The cost for extracting the atom is then associated to the energy required to fill the 4*f* band, rather than to the structural relaxation induced by the process. In the totally reduced Ce₂O₃, the extraction of O involves the transfer of 2e⁻ from the O 2*p* band to the Ce 4*f* valence band. Figures 8 shows the correlation between the reduction energies and the intra gap O 2*p* – Ce 4*f*. A linear direct correlation is observed for gap greater than 0.5 eV, whereas it is reversed for smaller band gap obtained with M05-2x and M06-HF.

3.6 Oxygen vacancy on the surface 111.

Because of the importance of surface defects on the catalytic properties of Ceria we have extended the benchmark also to the formation energy of an oxygen vacancy at the (111) CeO₂ surface. To this goal the HSE06 and 3 GHs with 25, 20 and 16 % of EE: PBE0, PW1PW91 and B1WC functionals have been chosen.

Figure 9 shows the slab model employed. An active oxide surface as the one considered here can transfers O atoms to a substrate following the mechanism proposed by Mars and van Krevelen⁷¹, with

the formation of a superficial oxygen vacancy and an oxygenated substrate. The surface vacancy can then be healed by the migration of a subsurface oxygen into the cavity, or in presence of partial pressure of O₂ or other oxygenated species, by the capture of the O by the vacancy⁷². Therefore, the cost of formation of an O vacancy is a good descriptor for the thermodynamics and the kinetics of these processes. When the O vacancy is modelled into the pristine bulk or surfaces of CeO₂, a reorganization of the excess of electron density left in the vacancy is observed. Driven by atomic relaxations of the defective sites environment, the excess of electron density localizes on the 4*f* states of the nearby Ce atoms, which are formally reduced to the open shell species Ce³⁺. Many configurations can be formed, with Ce³⁺ in different cationic coordination spheres with respect to the vacancy: in the first (nearest neighbour, nn), second (next nearest neighbour, nnn) and so on. The theoretical works of Pirovano et al⁵³ and Li et al⁷³ show that for the most stable surface, the (111), the most stable configurations are the ones with both the Ce³⁺ in nnn positions (nnn-nnn), followed by nnn_nn and then nn_nn. In addition, they find the vacancy in the second layer of O from the surface (subsurface vacancy) more stable than the vacancy in the outer layer (surface vacancy).

With our protocol, we have obtained only the nn_nn configurations for both kind of vacancies, with localization of the spin density on two of the three Ce next to the vacancy. Figure 10 depicts the two vacancies on the surface (111). The reason is that for the starting geometries, the localization on nn_nn is favourite compared to a localization at further sites from the vacancy. Then, the geometry optimization leads to a local minimum with the aforementioned configuration. Without manipulations on the starting geometries or without an artificial stabilization of the desired SCF solution, it is not possible to obtain the configurations with Ce³⁺ in nnn position.

Therefore, we limit the benchmark of xc functionals to the investigation of the nn_nn configurations. The main results concerning the relative stability of the surface/subsurface vacancies, energy of formation, spin localization on the Ce³⁺ sites, structural relaxation and electronic structure are reported in Table 5, whereas all the density of states for the pristine and defective structures can be found in the ESI, section 7.

The surface vacancy is predicted less stable than the subsurface one with all the functionals, in agreement with the results obtained with PBE+U and HSE06^{53,73}. However, the results for PBE0 contradicts the ones reported by Burow et al⁷⁴, who employing a Periodic Electrostatic Embedded Cluster method (PEECM) to simulate the isolated surface and subsurface vacancy, obtained the opposite order of stability. In the same work they also found the vacancy in the bulk ($E_{fv} = 3.00$ eV) more stable than the one on the surface, in contrast with many other results^{14,76} which found lower energies of formation for the surface vacancy. This discrepancy may be explained by the large core

ECP employed in their work for Ce, which has been proved by Kullgren et al¹⁷ to perform poorly for the Cerium Oxides, compared to the small core ECP.

The energy of formation for both types of vacancy follows the same trend observed for the reduction energy. This behaviour can be ascribed to the different weight of the EE: PBE0 predicts the smallest energies (3.00/2.77 eV for the surface and subsurface respectively), followed by HSE06 (3.10/2.88 eV), PW1PW91 (3.39/3.04) and B1WC (3.78/3.63). B1WC predicts the energy closest to the experimental value of 4.02 eV. However, it is expected that the computed energy of formation decrease when larger supercell models are used to simulate more diluted vacancy, in fact, according to the finding of Paier et al¹⁴ for HSE06 the energy decreases of 0.86/0.95 eV. The electronic structure of the two types of vacancies has slightly different features: the gap O 2*p* - Ce 4*f* (unoccupied) appears unchanged with respect to the pristine surface case, whereas the occupied Ce 4*f* state lies closer to the conduction band for the subsurface vacancy with respect to the superficial ones. The electronic structures of both vacancies show that the defective states are characterized by two sharp spikes assigned to the occupation of Ce 4*f* states upon localization on Ce (see section 9 in the ESI). The presence of two spikes is assigned to the crystal field splitting of the occupied Ce 4*f* states. These states are closer to the conduction for the subsurface vacancy with respect to the superficial one. The gap O 2*p* - Ce 4*f* (unoccupied), results almost unchanged compared to the one of the pristine slab. For the O vacancies in bulk Ceria, Kullgren et al³ have reported that occupied Ce 4*f* states lie at about 2 eV above the top of O 2*p* valence band and 1 eV from the conduction: assuming that this description hold for the surface 111, it is better reproduced by HSE06 and PW1PW91. As observed before, PBE0 overestimates the fundamental gap, while B1WC seems to underestimate it of at least 0.5 eV. Concerning the spin localization, a very qualitative description is obtained by the Mulliken analysis: for both vacancies, PBE0 gives the largest spin localization on the two formally reduced Ce³⁺ (1.000/1.000), while HSE06 and PW1PW91 localizes slightly less spin density at the surface (0.997 and 0.994, respectively), the minimum being reached by B1WC (0.969/0.962). The relaxation factor (R_f), computed as ratio between the average Ce³⁺-O distances for the defect and the average Ce-O distances in the relaxed pristine surface, show a larger relaxation for the subsurface vacancy, which explain the smaller energy of formation compared to the surface one. This factor increases with the weight of EE, being the smallest for B1WC (1.010/1.017) and largest for PBE0 (1.018/1.025) and reflect the degree of spin localization. These results show that among the xc functionals, the description of the localized nature of the defective states for the O vacancy on the 111 surface depends on the amount of EE in the xc functional. B1WC gives the worst description because the 16 % of EE is not enough to relieve the SIE from this system. PW1PW91 with 20 % of EE provides results very

similar to HSE06 and gives higher energy of formations. PBE0 gives the best localization, but again overestimate the band gap and gives the lowest energy of formation.

Conclusions

The structural, vibrational, electronic and thermochemical properties of the strong correlated ceria and Ce₂O₃ were investigated with different families of *xc* functionals.

From the initial evaluation of different GTO basis, the combination Ce2/O1 has emerged as the most balanced for the structural and electronic properties, however, the evaluation of more accurate thermochemical data requires the use of a more extensive combination, such as the Ce3/O2 one, proposed in this work.

The lattice parameters are reproduced within the 2% of deviation from the experimental values and are mainly dependent by the semi-local component of the exchange correlation terms. For the vibrational and elastic properties, the better agreement with experiments is obtained by the Global Hybrids and HSE06, while M-Global Hybrids and, to a lesser extent, Long Range Corrected Hybrids predict a more rigid structure, with a higher bulk modulus. The fraction of EE and its spatial partition highly affects the band gaps, which are overestimated by all the *xc* with fraction of EE above 20%, with the exception of the Short Range Corrected Hybrid. The weight of the EE affects also the reduction energies of CeO₂ to Ce₂O₃: the experimental values are better reproduced by local *xc* as PBE and M06L, which, however, perform much worse than hybrids for most of the other properties investigated. A strong correlation between the computed reduction energies and the intra gap O 2*p* - Ce 4*f* of Ce₂O₃ has been found.

Overall, *xc* functional with a percentage of EE between 16 and 25 give a good description of the investigated properties but it is not possible to identify the best performer.

The PBE0, PW1PW91, B1WC and HSE06 functionals used to study the O vacancy on the surface 111 of ceria predict the sub superficial vacancy more stable than the superficial one, but the geometry relaxations, the degree of localization of the spin density, the electronic structure and the energies of formation depend on the weight of the EE. For the study of the considered properties of the surface vacancies, PW1PW91 resulted the best performer, followed by HSE06.

ASSOCIATED CONTENT

Electronic Supporting Information

This material is available free of charge via the Internet at <http://pubs.acs.org> at the DOI

The GTO basis set employed, the main features of the xc functionals employed and the results of the basis set assessment are reported, as well all the numerical results obtained for the band gaps and the reduction reaction energy of the two oxides. All the DOSS of CeO₂, Ce₂O₃ and defective CeO₂ (111) are also reported.

Acknowledgments

A. P. thanks the University of Modena and Reggio-Emilia for supporting this work by granting the internal project (Fondo di Ateneo per la Ricerca, FAR2016) entitled “Innovative (oxide-based) materials and methods for fuel cell electrodes implementation”

References

- (1) Cohen, A. J.; Mori-Sánchez, P.; Yang, W. Challenges for Density Functional Theory. *Chem. Rev.* **2012**, *112*, 289–320.
- (2) Conesa, J. C. The Relevance of Dispersion Interactions for the Stability of Oxide Phases. *J. Phys. Chem. C* **2010**, *114*, 22718–22726.
- (3) Castleton, C. W. M.; Kullgren, J.; Hermansson, K. Tuning LDA+U for Electron Localization and Structure at Oxygen Vacancies in Ceria. *J. Chem. Phys.* **2007**, *127*, 244704.
- (4) Peverati, R.; Truhlar, D. G. Quest for a Universal Density Functional: The Accuracy of Density Functionals across a Broad Spectrum of Databases in Chemistry and Physics. *Philos. Trans. R. Soc. Math. Phys. Eng. Sci.* **2014**, *372* (2011), 20120476–20120476.
- (5) Dovesi, R.; Orlando, R.; Erba, A.; Zicovich-Wilson, C. M.; Civalleri, B.; Casassa, S.; Maschio, L.; Ferrabone, M.; De La Pierre, M.; D’Arco, P.; et al. CRYSTAL14: A Program for the Ab Initio Investigation of Crystalline Solids. *Int. J. Quantum Chem.* **2014**, *114*, 1287–1317.
- (6) Montini, T.; Melchionna, M.; Monai, M.; Fornasiero, P. Fundamentals and Catalytic Applications of CeO₂-Based Materials. *Chem. Rev.* **2016**, *116*, 5987–6041.
- (7) Svelle, S.; Tuma, C.; Rozanska, X.; Kerber, T.; Sauer, J. Quantum Chemical Modeling of Zeolite-Catalyzed Methylation Reactions: Toward Chemical Accuracy for Barriers. *J. Am. Chem. Soc.* **2009**, *131*, 816–825.
- (8) Seidl, A.; Görling, A.; Vogl, P.; Majewski, J. A.; Levy, M. Generalized Kohn-Sham Schemes and the Band-Gap Problem. *Phys. Rev. B* **1996**, *53*, 3764.
- (9) Da Silva, J. L. F.; Ganduglia-Pirovano, M. V.; Sauer, J.; Bayer, V.; Kresse, G. Hybrid Functionals Applied to Rare-Earth Oxides: The Example of Ceria. *Phys. Rev. B* **2007**, *75*.
- (10) Migani, A.; Vayssilov, G. N.; Bromley, S. T.; Illas, F.; Neyman, K. M. Dramatic Reduction of the Oxygen Vacancy Formation Energy in Ceria Particles: A Possible Key to Their Remarkable Reactivity at the Nanoscale. *J. Mater. Chem.* **2010**, *20*, 10535.
- (11) Fabris, S.; Vicario, G.; Balducci, G.; de Gironcoli, S.; Baroni, S. Electronic and Atomistic Structures of Clean and Reduced Ceria Surfaces. *J. Phys. Chem. B* **2005**, *109*, 22860–22867.
- (12) Nolan, M.; Grigoleit, S.; Sayle, D. C.; Parker, S. C.; Watson, G. W. Density Functional Theory Studies of the Structure and Electronic Structure of Pure and Defective Low Index Surfaces of Ceria. *Surf. Sci.* **2005**, *576*, 217–229.
- (13) Nolan, M. Hybrid Density Functional Theory Description of Oxygen Vacancies in the CeO₂ (110) and (100) Surfaces. *Chem. Phys. Lett.* **2010**, *499*, 126–130.
- (14) Paier, J.; Penschke, C.; Sauer, J. Oxygen Defects and Surface Chemistry of Ceria: Quantum Chemical Studies Compared to Experiment. *Chem. Rev.* **2013**, *113*, 3949–3985.
- (15) Hay, P. J.; Martin, R. L.; Uddin, J.; Scuseria, G. E. Theoretical Study of CeO₂ and Ce₂O₃ Using a Screened Hybrid Density Functional. *J. Chem. Phys.* **2006**, *125*, 034712.
- (16) D. Becke, A. Density-Functional Thermochemistry. III. The Role of Exact Exchange. *J. Chem. Phys.* **1993**, *98*, 5648–5653.
- (17) Kullgren, J.; Castleton, C. W. M.; Müller, C.; Ramo, D. M.; Hermansson, K. B3LYP Calculations of Cerium Oxides. *J. Chem. Phys.* **2010**, *132*, 054110.
- (18) Graciani, J.; Márquez, A. M.; Plata, J. J.; Ortega, Y.; Hernández, N. C.; Meyer, A.; Zicovich-Wilson, C. M.; Sanz, J. F. Comparative Study on the Performance of Hybrid DFT Functionals in Highly Correlated Oxides: The Case of CeO₂ and Ce₂O₃. *J. Chem. Theory Comput.* **2011**, *7*, 56–65.
- (19) Becke, A. D. A New Mixing of Hartree–Fock and Local Density-functional Theories. *J. Chem. Phys.* **1993**, *98*, 1372–1377.
- (20) Adamo, C.; Barone, V. Toward Reliable Density Functional Methods without Adjustable Parameters: The PBE0 Model. *J. Chem. Phys.* **1999**, *110*, 6158–6170.

- (21) Bilc, D. I.; Orlando, R.; Shaltaf, R.; Rignanese, G.-M.; Íñiguez, J.; Ghosez, P. Hybrid Exchange-Correlation Functional for Accurate Prediction of the Electronic and Structural Properties of Ferroelectric Oxides. *Phys. Rev. B* **2008**, *77*, 1-13.
- (22) Désaunay, T.; Ringuedé, A.; Cassir, M.; Labat, F.; Adamo, C. Modeling Basic Components of Solid Oxide Fuel Cells Using Density Functional Theory: Bulk and Surface Properties of CeO₂. *Surf. Sci.* **2012**, *606*, 305–311.
- (23) Evarestov, R. A.; Gryaznov, D.; Arrigoni, M.; Kotomin, E. A.; Chesnokov, A.; Maier, J. Use of Site Symmetry in Supercell Models of Defective Crystals: Polarons in CeO₂. *Phys. Chem. Chem. Phys.* **2017**, *19*, 8340–8348.
- (24) Yanai, T.; Tew, D. P.; Handy, N. C. A New Hybrid Exchange-Correlation Functional Using the Coulomb-Attenuating Method (CAM-B3LYP). *Chem. Phys. Lett.* **2004**, *393* (1–3), 51–57.
- (25) Perdew, J. P.; Burke, K.; Ernzerhof, M. Generalized Gradient Approximation Made Simple. *Phys. Rev. Lett.* **1996**, *77*, 3865–3868.
- (26) Zhao, Y.; Truhlar, D. G. A New Local Density Functional for Main-Group Thermochemistry, Transition Metal Bonding, Thermochemical Kinetics, and Noncovalent Interactions. *J. Chem. Phys.* **2006**, *125*, 194101.
- (27) Zhao, Y.; Schultz, N. E.; Truhlar, D. G. Exchange-Correlation Functional with Broad Accuracy for Metallic and Nonmetallic Compounds, Kinetics, and Noncovalent Interactions. *J. Chem. Phys.* **2005**, *123*, 161103.
- (28) Zhao, Y.; Schultz, N. E.; Truhlar, D. G. Design of Density Functionals by Combining the Method of Constraint Satisfaction with Parametrization for Thermochemistry, Thermochemical Kinetics, and Noncovalent Interactions. *J. Chem. Theory Comput.* **2006**, *2*, 364–382.
- (29) Zhao, Y.; Truhlar, D. G. The M06 Suite of Density Functionals for Main Group Thermochemistry, Thermochemical Kinetics, Noncovalent Interactions, Excited States, and Transition Elements: Two New Functionals and Systematic Testing of Four M06-Class Functionals and 12 Other Functionals. *Theor. Chem. Acc.* **2008**, *120*, 215–241.
- (30) Perdew, J. P.; Yue, W. Accurate and Simple Density Functional for the Electronic Exchange Energy: Generalized Gradient Approximation. *Phys. Rev. B* **1986**, *33*, 8800-8802.
- (31) Guido, C. A.; Brémond, E.; Adamo, C.; Cortona, P. Communication: One Third: A New Recipe for the PBE0 Paradigm. *J. Chem. Phys.* **2013**, *138*, 021104.
- (32) Perdew, J. P.; Ruzsinszky, A.; Csonka, G. I.; Vydrov, O. A.; Scuseria, G. E.; Constantin, L. A.; Zhou, X.; Burke, K. Restoring the Density-Gradient Expansion for Exchange in Solids and Surfaces. *Phys. Rev. Lett.* **2008**, *100*, 136406
- (33) Bredow, T.; Gerson, A. R. Effect of Exchange and Correlation on Bulk Properties of MgO, NiO, and CoO. *Phys. Rev. B* **2000**, *61*, 5194.
- (34) Demichelis, R.; Civalleri, B.; Ferrabone, M.; Dovesi, R. On the Performance of Eleven DFT Functionals in the Description of the Vibrational Properties of Aluminosilicates: Performance of Eleven DFT Functionals. *Int. J. Quantum Chem.* **2010**, *110*, 406–415.
- (35) Chai, J.-D.; Head-Gordon, M. Systematic Optimization of Long-Range Corrected Hybrid Density Functionals. *J. Chem. Phys.* **2008**, *128*, 084106.
- (36) Hamprecht, F. A.; Cohen, A. J.; Tozer, D. J.; Handy, N. C. Development and Assessment of New Exchange-Correlation Functionals. *J. Chem. Phys.* **1998**, *109*, 6264–6271.
- (37) Krukau, A. V.; Vydrov, O. A.; Izmaylov, A. F.; Scuseria, G. E. Influence of the Exchange Screening Parameter on the Performance of Screened Hybrid Functionals. *J. Chem. Phys.* **2006**, *125*, 224106.
- (38) Schimka, L.; Harl, J.; Kresse, G. Improved Hybrid Functional for Solids: The HSEsol Functional. *J. Chem. Phys.* **2011**, *134*, 024116.
- (39) Henderson, T. M.; Izmaylov, A. F.; Scuseria, G. E.; Savin, A. Assessment of a Middle-Range Hybrid Functional. *J. Chem. Theory Comput.* **2008**, *4*, 1254–1262.

- (40) Henderson, T. M.; Izmaylov, A. F.; Scuseria, G. E.; Savin, A. The Importance of Middle-Range Hartree-Fock-Type Exchange for Hybrid Density Functionals. *J. Chem. Phys.* **2007**, *127*, 221103.
- (41) Vydrov, O. A.; Scuseria, G. E. Assessment of a Long-Range Corrected Hybrid Functional. *J. Chem. Phys.* **2006**, *125*, 234109.
- (42) Weintraub, E.; Henderson, T. M.; Scuseria, G. E. Long-Range-Corrected Hybrids Based on a New Model Exchange Hole. *J. Chem. Theory Comput.* **2009**, *5*, 754–762.
- (43) Vosko, S. H.; Wilk, L.; Nusair, M. Accurate Spin-Dependent Electron Liquid Correlation Energies for Local Spin Density Calculations: A Critical Analysis. *Can. J. Phys.* **1980**, *58* (8), 1200–1211.
- (44) Gerber, I. C.; Ángyán, J. G. London Dispersion Forces by Range-Separated Hybrid Density Functional with Second Order Perturbational Corrections: The Case of Rare Gas Complexes. *J. Chem. Phys.* **2007**, *126*, 044103.
- (45) Becke, A. D. Density-Functional Thermochemistry. V. Systematic Optimization of Exchange-Correlation Functionals. *J. Chem. Phys.* **1997**, *107*, 8554–8560.
- (46) Dolg, M.; Stoll, H.; Savin, A.; Preuss, H. Energy-Adjusted Pseudopotentials for the Rare Earth Elements. *Theor. Chem. Acc. Theory Comput. Model. Theor. Chim. Acta* **1989**, *75*, 173–194.
- (47) Cao, X.; Dolg, M. Segmented Contraction Scheme for Small-Core Lanthanide Pseudopotential Basis Sets. *J. Mol. Struct. THEOCHEM* **2002**, *581*, 139–147.
- (48) Thakkar, A. J.; Koga, T.; Saito, M.; Hoffmeyer, R. E. Double and Quadruple Zeta Contracted Gaussian Basis Sets for Hydrogen through Neon. *Int. J. Quantum Chem.* **1993**, *48*, 343–354.
- (49) Peintinger, M. F.; Oliveira, D. V.; Bredow, T. Consistent Gaussian Basis Sets of Triple-Zeta Valence with Polarization Quality for Solid-State Calculations. *J. Comput. Chem.* **2013**, *34*, 451–459.
- (50) Pinto, H.; Mintz, M. H.; Melamud, M.; Shaked, H. Neutron Diffraction Study of Ce₂O₃. *Phys. Lett. A* **1982**, *88*, 81–83.
- (51) Perger, W. F.; Criswell, J.; Civalleri, B.; Dovesi, R. Ab-Initio Calculation of Elastic Constants of Crystalline Systems with the CRYSTAL Code. *Comput. Phys. Commun.* **2009**, *180*, 1753–1759.
- (52) Erba, A.; Mahmoud, A.; Orlando, R.; Dovesi, R. Elastic Properties of Six Silicate Garnet End Members from Accurate Ab Initio Simulations. *Phys. Chem. Miner.* **2014**, *41* (2), 151–160.
- (53) Ganduglia-Pirovano, M. V.; Da Silva, J. L. F.; Sauer, J. Density-Functional Calculations of the Structure of Near-Surface Oxygen Vacancies and Electron Localization on CeO₂ (111). *Phys. Rev. Lett.* **2009**, *102*, 026101.
- (54) Torbrügge, S.; Reichling, M.; Ishiyama, A.; Morita, S.; Custance, Ó. Evidence of Subsurface Oxygen Vacancy Ordering on Reduced CeO₂ (111). *Phys. Rev. Lett.* **2007**, *99*, 056101.
- (55) Gerward, L.; Olsen, J. S. Powder Diffraction Analysis of Cerium Dioxide at High Pressure. *Powder Diffr.* **1993**, *8*, 127–129.
- (56) Castleton, C. W. M.; Kullgren, J.; Hermansson, K. Tuning LDA+U for Electron Localization and Structure at Oxygen Vacancies in Ceria. *J. Chem. Phys.* **2007**, *127*, 244704
- (57) Paier, J.; Marsman, M.; Kresse, G. Why Does the B3LYP Hybrid Functional Fail for Metals? *J. Chem. Phys.* **2007**, *127*, 024103.
- (58) Lipp, M. J.; Jeffries, J. R.; Cynn, H.; Park Klepeis, J.-H.; Evans, W. J.; Mortensen, D. R.; Seidler, G. T.; Xiao, Y.; Chow, P. Comparison of the High-Pressure Behavior of the Cerium Oxides Ce₂O₃ and CeO₂. *Phys. Rev. B* **2016**, *93*, 064106.
- (59) M. J. Frisch, G. W. Trucks, H. B. Schlegel, G. E. Scuseria, M.A. Robb, J. R. Cheeseman, G. Scalmani, V. Barone, B. Mennucci, G. A. Petersson, H. Nakatsuji, M. Caricato, X. Li, H. P. Hratchian, A. F. Izmaylov, J. Bloino, G. Zheng, J. L. Sonnenberg, M. Hada, M. Ehara, K. Toyota, R. Fukuda, J. Hasegawa, M. Ishida, T. Nakajima, Y. Honda, O. Kitao, H. Nakai, T. Vreven, J. A. Montgomery, Jr., J. E. Peralta, F. Ogliaro, M. Bearpark, J. J. Heyd, E. Brothers, K. N. Kudin, V. N. Staroverov, R.

- Kobayashi, J. Normand, K. Raghavachari, A. Rendell, J. C. Burant, S. S. Iyengar, J. Tomasi, M. Cossi, N. Rega, J. M. Millam, M. Klene, J. E. Knox, J. B. Cross, V. Bakken, C. Adamo, J. Jaramillo, R. Gomperts, R. E. Stratmann, O. Yazyev, A. J. Austin, R. Cammi, C. Pomelli, J. W. Ochterski, R. L. Martin, K. Morokuma, V. G. Zakrzewski, G. A. Voth, P. Salvador, J. J. Dannenberg, S. Dapprich, A. D. Daniels, Ö. Farkas, J. B. Foresman, J. V. Ortiz, J. Cioslowski, and D. J. Fox, Gaussian 09, revision D.01; Gaussian, Inc.: Wallingford, CT, 2013
- (60) Pernot, P.; Civalleri, B.; Presti, D.; Savin, A. Prediction Uncertainty of Density Functional Approximations for Properties of Crystals with Cubic Symmetry. *J. Phys. Chem. A* **2015**, *119*, 5288–5304.
- (61) Perdew, J. P.; Yang, W.; Burke, K.; Yang, Z.; Gross, E. K.; Scheffler, M.; Scuseria, G. E.; Henderson, T. M.; Zhang, I. Y.; Ruzsinszky, A. Understanding Band Gaps of Solids in Generalized Kohn–Sham Theory. *Proc. Natl. Acad. Sci.* **2017**, *114*, 2801–2806.
- (62) Prokofiev, A. V.; Shelykh, A. I.; Melekh, B. T. Periodicity in the Band Gap Variation of Ln_2X_3 (X = O, S, Se) in the Lanthanide Series. *Journal of Alloys and Compounds* **1996**, *242*, 41–44.
- (63) Tran, F.; Blaha, P. Importance of the Kinetic Energy Density for Band Gap Calculations in Solids with Density Functional Theory. *J. Phys. Chem. A* **2017**, *121*, 3318–3325.
- (64) Tran, F.; Blaha, P. Accurate Band Gaps of Semiconductors and Insulators with a Semilocal Exchange–Correlation Potential. *Phys. Rev. Lett.* **2009**, *102*, 226401.
- (65) Andersson, D. A.; Simak, S. I.; Johansson, B.; Abrikosov, I. A.; Skorodumova, N. V. Modeling of CeO_2 , Ce_2O_3 , CeO_{2-x} in the LDA+U Formalism. *Phys. Rev. B* **2007**, *75*, 035109.
- (66) Fabris, S.; de Gironcoli, S.; Baroni, S.; Vicario, G.; Balducci, G. Taming Multiple Valency with Density Functionals: A Case Study of Defective Ceria. *Phys. Rev. B* **2005**, *71*, 041102.
- (67) Schilling, C.; Hofmann, A.; Hess, C.; Ganduglia-Pirovano, M. V. Raman Spectra of Polycrystalline CeO_2 : A Density Functional Theory Study. *J. Phys. Chem. C* **2017**, *121*, 20834–20849.
- (68) Avisar, D.; Livneh, T. The Raman-Scattering of A-Type Ce_2O_3 . *Vib. Spectrosc.* **2016**, *86*, 14–16.
- (69) Zinkevich, M.; Djurovic, D.; Aldinger, F. Thermodynamic Modelling of the Cerium–Oxygen System. *Solid State Ion.* **2006**, *177*, 989–1001.
- (70) Pacchioni, G. Modeling Doped and Defective Oxides in Catalysis with Density Functional Theory Methods: Room for Improvements. *J. Chem. Phys.* **2008**, *128*, 182505.
- (71) Mars, P.; Van Krevelen, D. W. Oxidations Carried out by Means of Vanadium Oxide Catalysts. *Chem. Eng. Sci.* **1954**, *3*, 41–59.
- (72) Huang, M.; Fabris, S. Role of Surface Peroxo and Superoxo Species in the Low-Temperature Oxygen Buffering of Ceria: Density Functional Theory Calculations. *Phys. Rev. B* **2007**, *75*, 081404.
- (73) Li, H.-Y.; Wang, H.-F.; Gong, X.-Q.; Guo, Y.-L.; Guo, Y.; Lu, G.; Hu, P. Multiple Configurations of the Two Excess 4f Electrons on Defective CeO_2 (111): Origin and Implications. *Phys. Rev. B* **2009**, *79*, 193401.
- (74) Burow, A. M.; Sierka, M.; Döbler, J.; Sauer, J. Point Defects in CaF_2 and CeO_2 Investigated by the Periodic Electrostatic Embedded Cluster Method. *J. Chem. Phys.* **2009**, *130*, 174710.
- (75) Ganduglia-Pirovano, M. V. Oxygen Defects at Reducible Oxide Surfaces: The Example of Ceria and Vanadia. In *Defects at Oxide Surfaces*; Jupille, J., Thornton, G., Eds.; Springer International Publishing: Cham, 2015; Vol. 58, pp 149–190.
- (76) Gerward, L.; Staun Olsen, J.; Petit, L.; Vaitheeswaran, G.; Kanchana, V.; Svane, A. Bulk Modulus of CeO_2 and PrO_2 —An Experimental and Theoretical Study. *J. Alloys Compd.* **2005**, *400*, 56–61.

- (77) Duclos, S. J.; Vohra, Y. K.; Ruoff, A. L.; Jayaraman, A.; Espinosa, G. P. High-Pressure x-Ray Diffraction Study of CeO₂ to 70 GPa and Pressure-Induced Phase Transformation from the Fluorite Structure. *Phys. Rev. B* **1988**, *38*, 7755.
- (78) Rossignol, S.; Gérard, F.; Mesnard, D.; Kappenstein, C.; Duprez, D. Structural Changes of Ce–Pr–O Oxides in Hydrogen: A Study by in Situ X-Ray Diffraction and Raman Spectroscopy. *J. Mater. Chem.* **2003**, *13*, 3017–3020.
- (79) Nakajima, A.; Yoshihara, A.; Ishigame, M. Defect-Induced Raman Spectra in Doped CeO₂. *Phys. Rev. B* **1994**, *50*, 13297.
- (80) Bärnighausen, H.; Schiller, G. The Crystal Structure of A-Ce₂O₃. *J. Common Met.* **1985**, *110*, 385–390.
- (81) Mochizuki, S. Infrared Optical Properties of Cerium Dioxide. *Phys. Status Solidi B* **1982**, *114*, 189–199.
- (82) Clausen, K.; Hayes, W.; Macdonald, J. E.; Osborn, R.; Schnabel, P. G.; Hutchings, M. T.; Magerl, A. Inelastic Neutron Scattering Investigation of the Lattice Dynamics of ThO₂ and CeO₂. *J. Chem. Soc. Faraday Trans. 2 Mol. Chem. Phys.* **1987**, *83*, 1109–1112.
- (83) Weber, W. H.; Hass, K. C.; McBride, J. R. Raman Study of CeO₂: Second-Order Scattering, Lattice Dynamics, and Particle-Size Effects. *Phys. Rev. B* **1993**, *48*, 178–185.
- (84) Kourouklis, G. A.; Jayaraman, A.; Espinosa, G. P. High-Pressure Raman Study of CeO₂ to 35 GPa and Pressure-Induced Phase Transformation from the Fluorite Structure. *Phys. Rev. B* **1988**, *37*, 4250–4253.

Figures

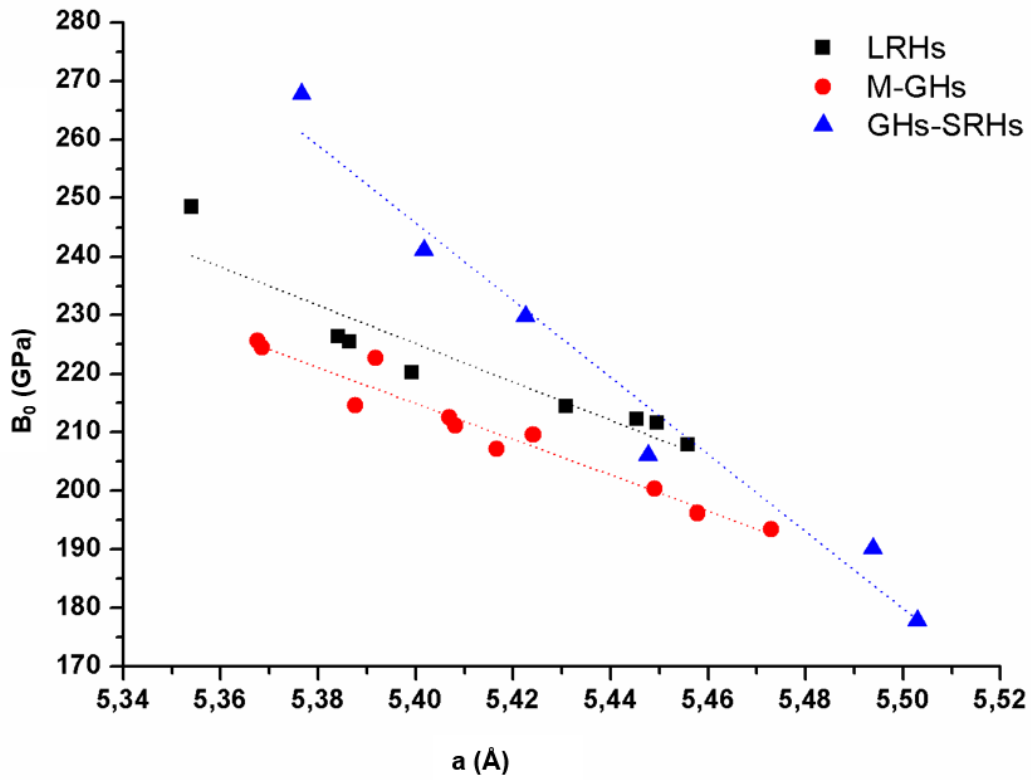


Figure 1: Plot of the Bulk Modulus B_0 vs lattice parameter a of ceria for the different family of functionals. PBE and M06L were included in the GHs and M-GHs respectively as special cases with EE contributions equal to zero.

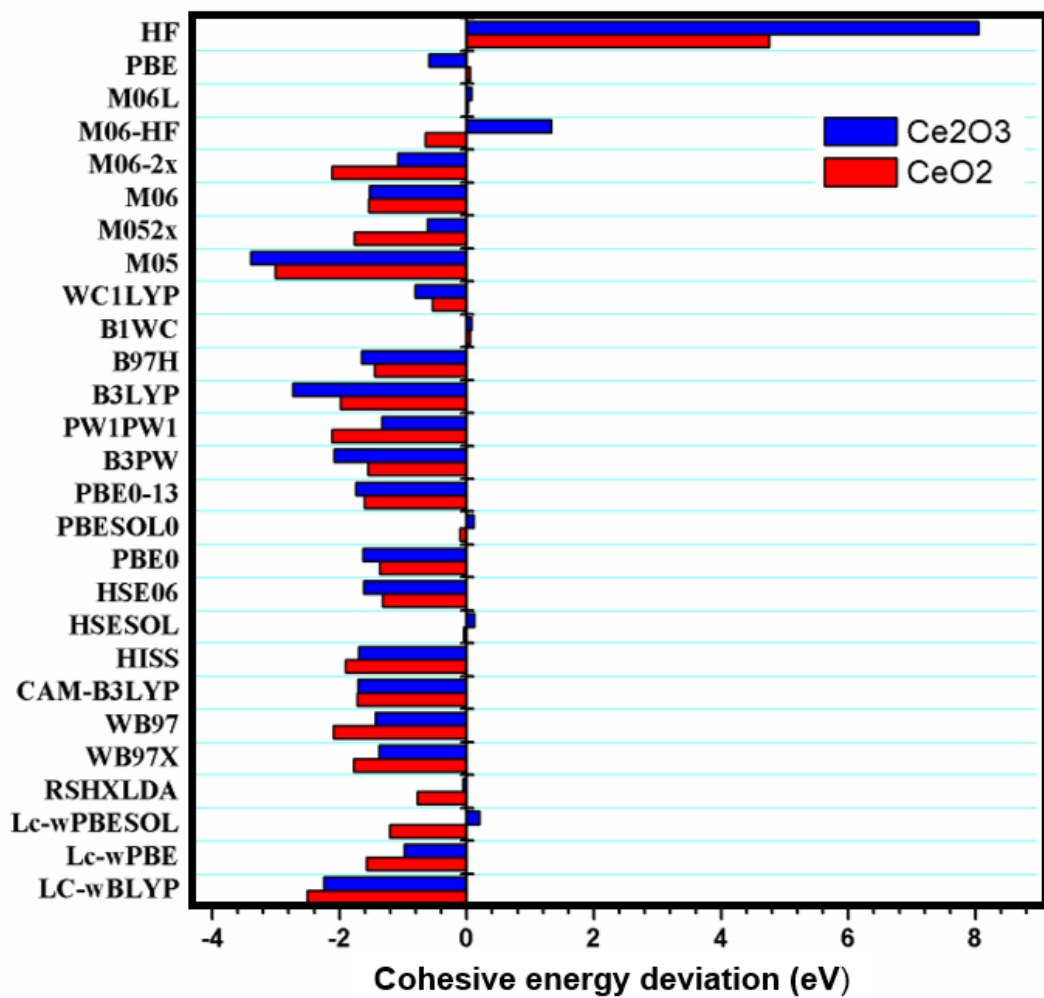


Figure 2: Differences between tabulated and calculated cohesive energies per unit cell of CeO₂ and Ce₂O₃.

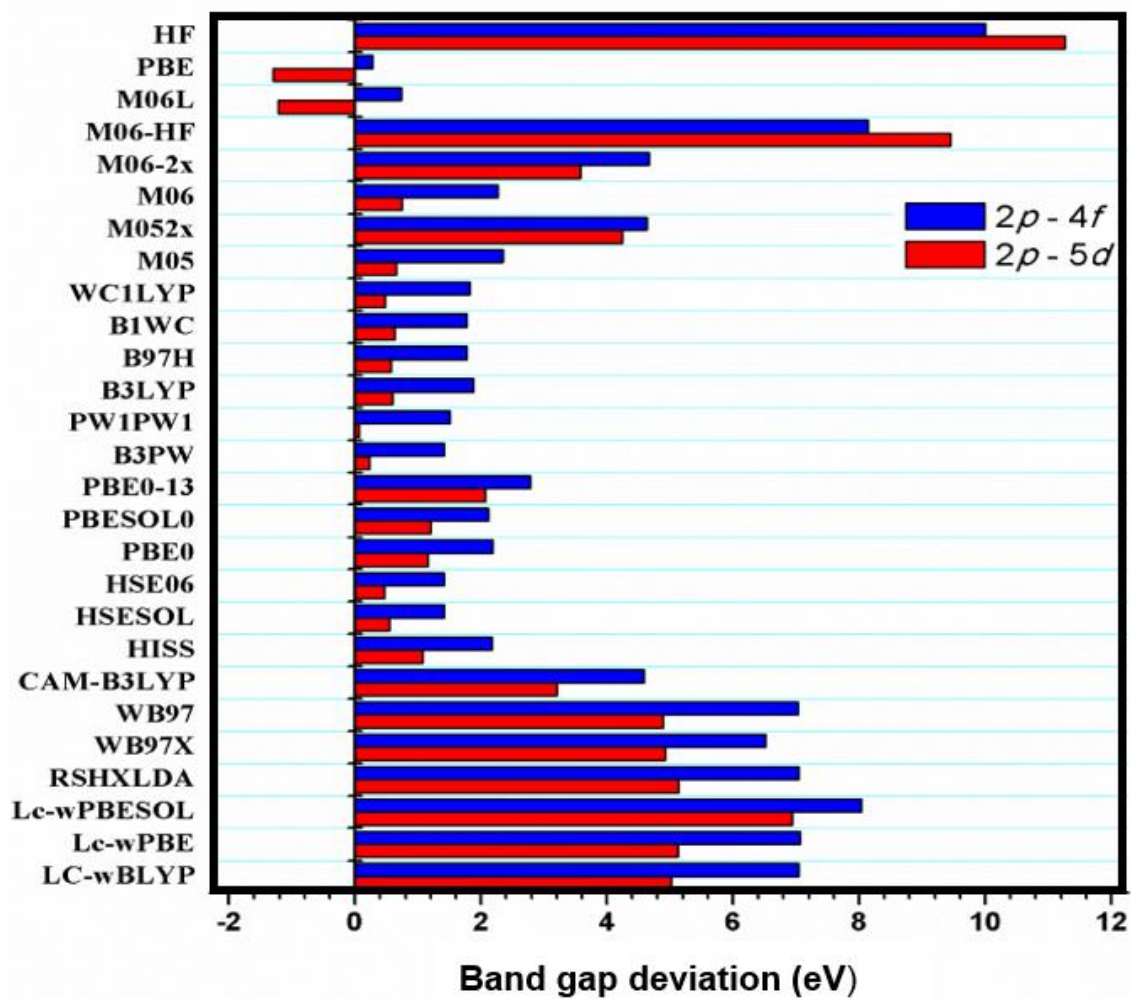


Figure 3. Difference between the calculated Kohn Sham band gaps and the experimental O $2p$ – Ce $4f$ (blue) and O $2p$ - Ce $5d$ (red) gaps for CeO₂. The difference has been computed with respect to the commonly used value of 3 and 6 eV.

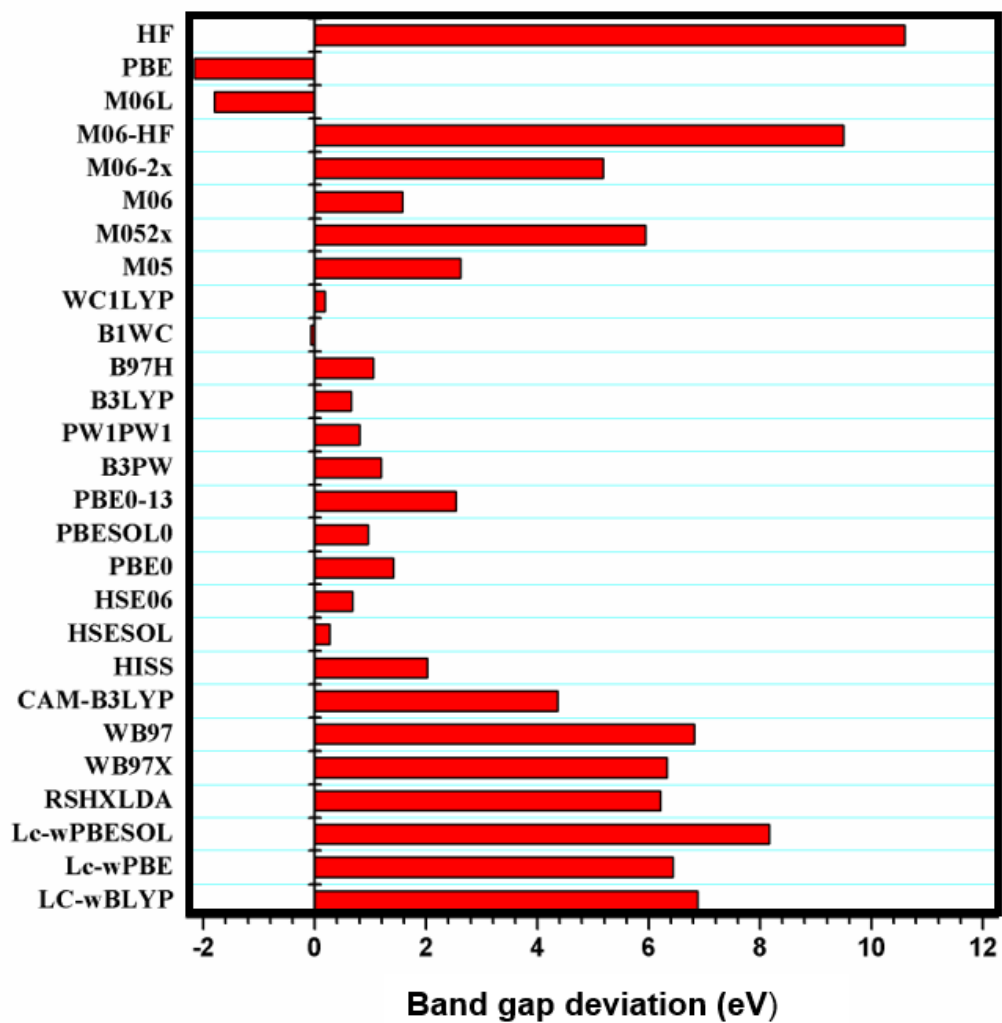


Figure 4. Difference between the calculated Kohn Sham band gap and the experimental optical gap (2.4 eV) for Ce_2O_3 .

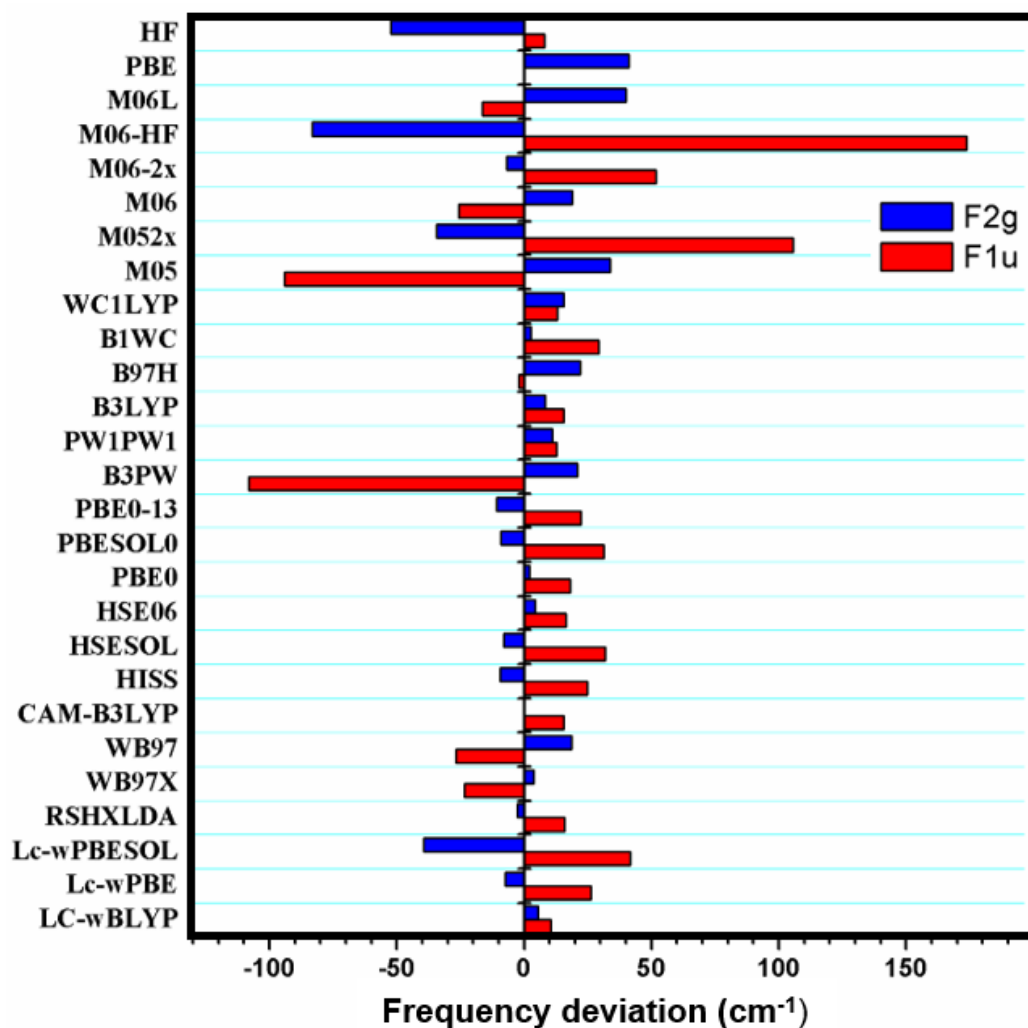


Figure 5. Calculated harmonic frequencies at the Γ point minus experimental frequencies of CeO_2 . Only the interval of plus and minus 30 cm^{-1} is represented to magnify the smaller differences.

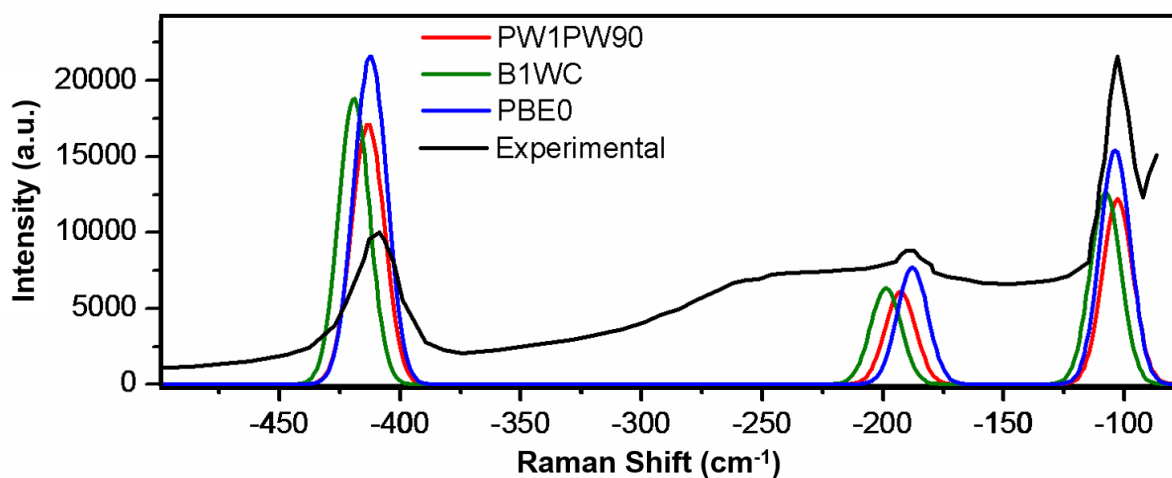


Figure 6: Simulated PBE0, B1WC and PW1PW91 Raman spectra of Ce_2O_3 compared with the experimental spectrum digitalized from ref 68. Calculated intensities were scaled to match the highest intensity experimental peak and convoluted with Gaussian functions. A standard band width of 15 cm^{-1} has been applied.

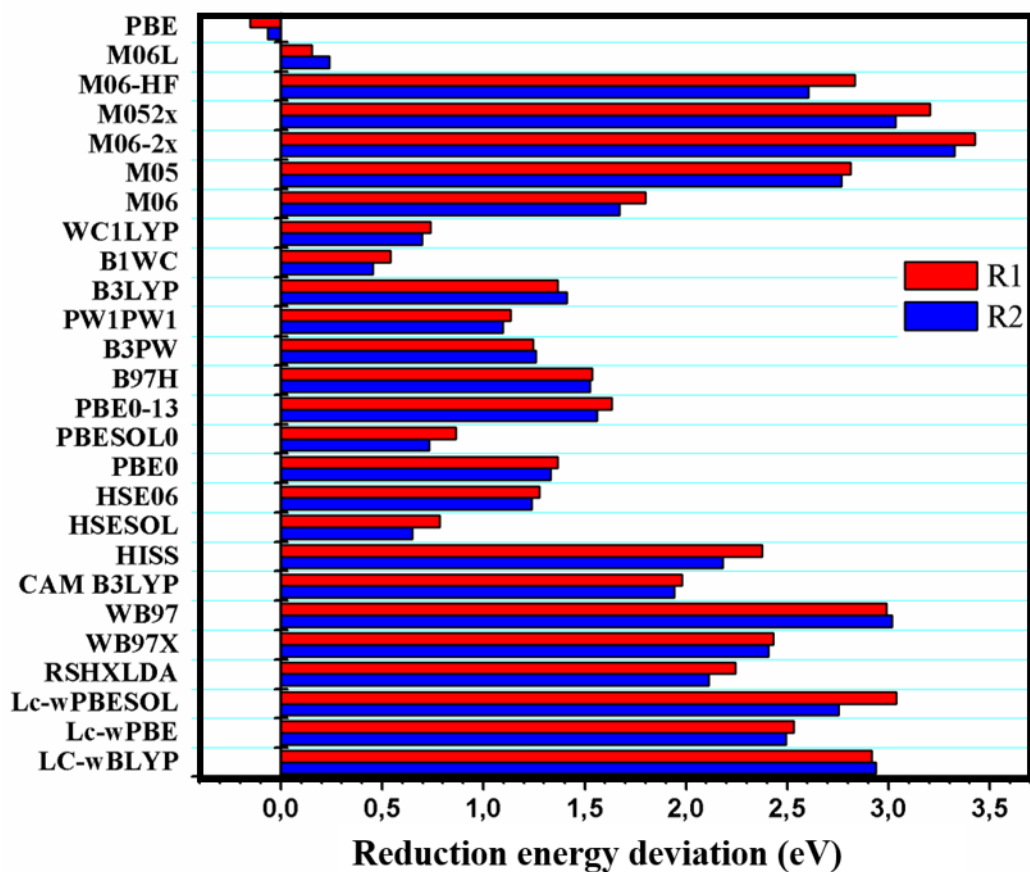


Figure 7: Deviation from the experimental values of the reaction energies of CeO_2 to Ce_2O_3 according the R1 ($\Delta H(R1)=4.02$ eV) and R2 ($\Delta H(R2)=1.54$ eV). Zero Point Energy contributions were not considered.

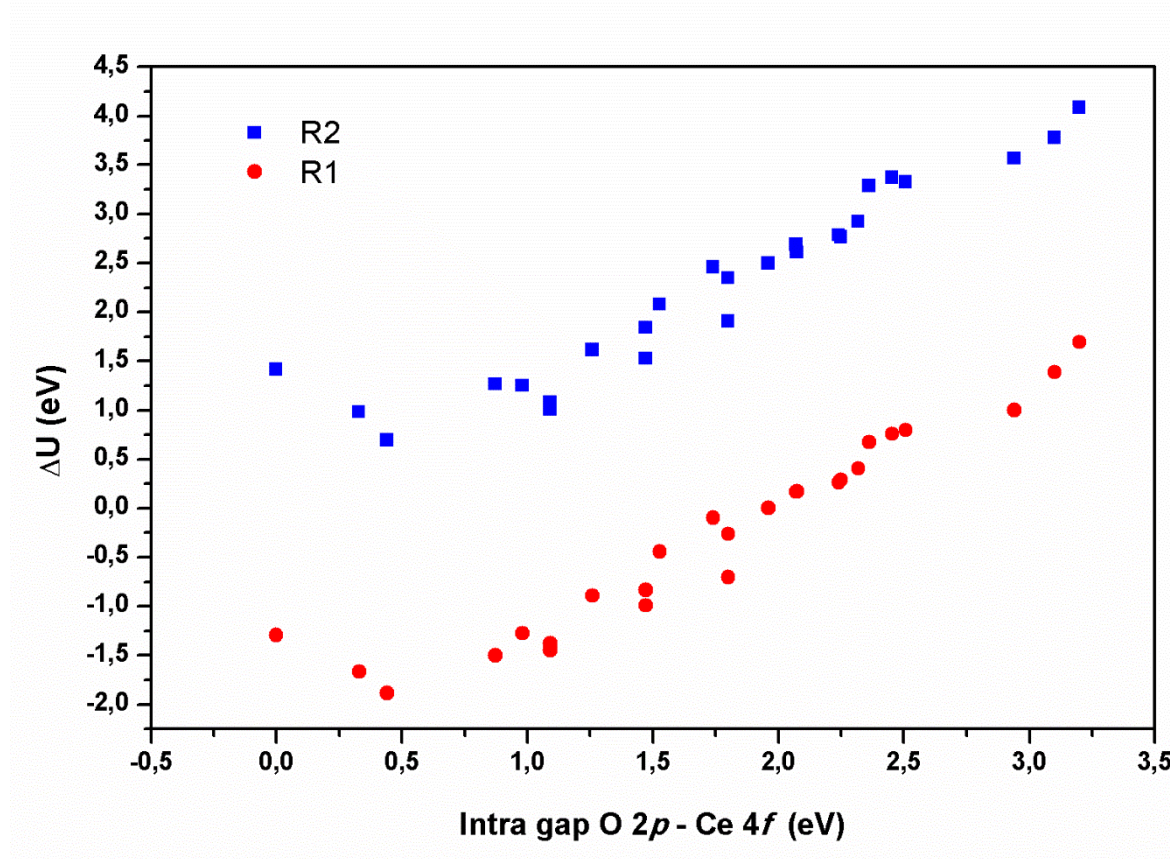


Figure 8: Correlation between the reduction energies ΔU R1 and ΔU R2 and the intra gap O $2p$ - Ce $4f$ (occupied) in Ce_2O_3 for R1(a) and R2(b).

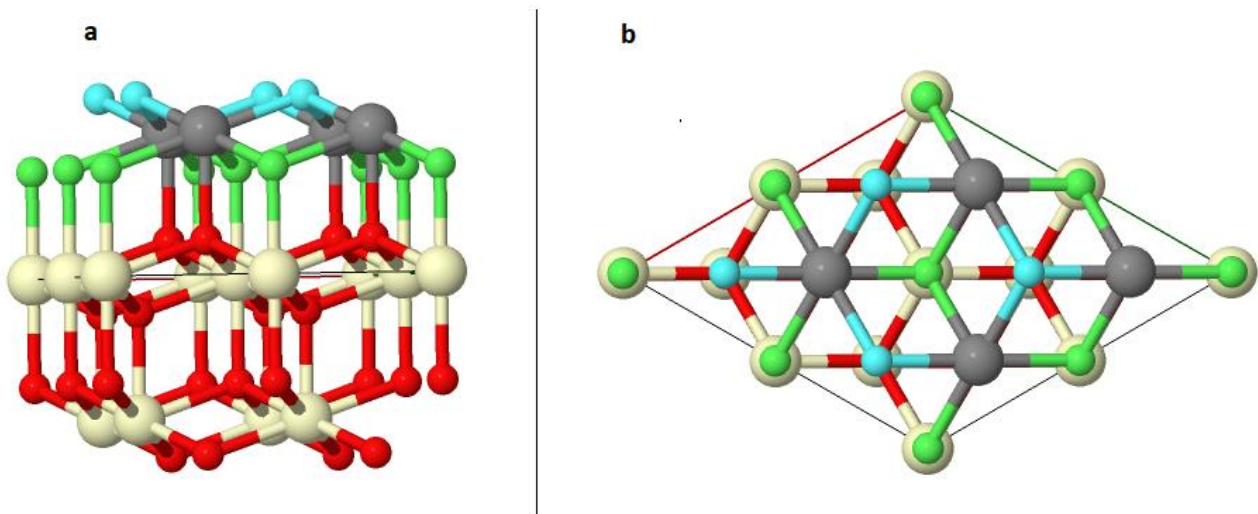


Figure 9: Side (a) and top (b) view of the CeO_2 111 $p(2 \times 2)$ slab. The superficial layer of O is represented in light blue, the sub-superficial layer of O in light green. Between the two, the Ce layer in grey. The underneath layers of O and Ce are represented in red and white respectively.

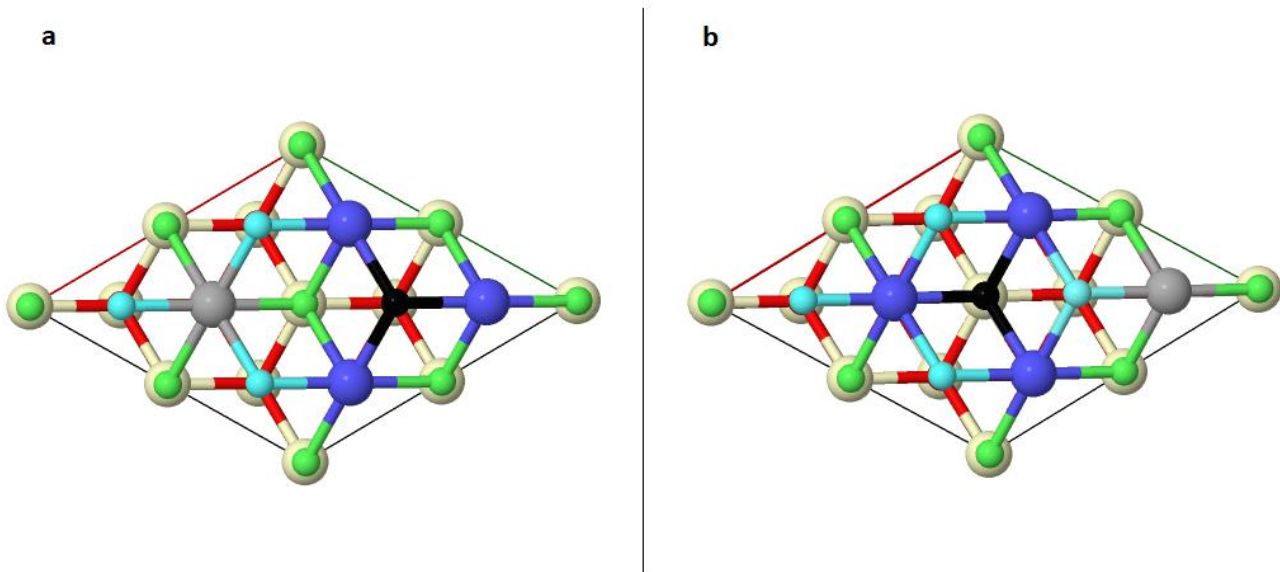


Figure 10: The modelled vacancy in the superficial O layer (a) and in the sub superficial O layer (b). The vacant O is coloured in black for both cases. The three Ce atoms in the first cationic shell of the vacancy (nearest neighbours, nns) are represented in cyan. Ce atoms in the second cationic sphere of the vacancy (next nearest neighbour, nnn) are represented in grey.

Tables

Table 1. Computed cell parameter, bulk modulus and independent elastic tensor components for CeO₂.

Method	a(Å)	B ₀ (GPa)	c11(GPa)	c21(GPa)	c44(GPa)
Experimental	5.411 ⁷⁶ 5.406 ⁷⁷ 5.390 ⁷⁸	20479-220 ⁷⁶ - 230 ⁷⁹ -236 ⁷⁷	40379	10579	6079
CAM-B3LYP	5.431	214.4	417.8	112.7	59.7
LC-ωBLYP	5.445	212.3	417.3	109.8	52.6
Lc-ωPBE	5.384	226.3	438.2	120.3	59.7
Lc-ωPBEsol	5.354	248.5	482.0	131.8	78.4
RSHXLDA	5.399	220.2	432.2	114.2	59.5
HISS	5.387	225.4	436.7	119.8	66.6
ωB97X	5.450	211.6	418.6	108.1	48.6
ωB97	5.456	207.8	418.0	102.7	41.1
HSEsol	5.368	224.5	426.4	123.5	68.9
HSE06	5.408	211.2	408.0	112.8	61.2
PBE0	5.407	212.6	411.3	113.3	61.7
PBEsol0	5.368	225.7	429.4	123.8	69.3
PBE0-13	5.392	222.7	432.3	117.8	65.8
B1WC	5.388	214.6	404.9	119.4	65.5
WC1LYP	5.449	200.3	383.0	108.9	59.0
B97H	5.458	196.2	377.7	105.5	56.8
B3PW91	5.424	209.5	405.5	111.5	60.5
PW1PW91	5.417	207.1	398.6	111.4	59.7
B3LYP	5.473	193.5	378.8	100.8	53.0
M06L	5.503	177.8	343.8	94.8	45.1
M06	5.448	206.1	397.3	110.5	42.9
M06-2x	5.423	229.8	439.9	124.8	62.8
M06-HF	5.377	267.8	497.5	153.0	117.9
M05	5.494	190.2	375.8	97.4	36.0
M052x	5.402	241.1	457.5	132.9	87.3
PBE	5.471	176.9	337.3	96.7	51.0
HF	5.470	228.2	469.2	107.7	83.7

Table 2. Computed cell parameter, bulk modulus and independents elastic tensor component for Ce_2O_3

Method	a(Å)	c(Å)	c/a	B_0 (H) (GPa)	C_{11} (GPa)	C_{12} (GPa)	C_{13} (GPa)	C_{33} (GPa)	C_{44} (GPa)
Experimental	3.891 ⁸⁰	6.059 ⁸⁰	1.56	111 ⁸¹					
CAM-B3LYP	3.883	6.143	1.582	135.6	236.4	135.4	92.1	157.2	72.5
LC-ωBLYP	3.896	6.192	1.589	132.4	231.7	130.7	89.5	154.8	73.0
Lc-ωPBE	3.866	6.034	1.561	139.4	247.1	139.4	96.9	155.3	80.8
Lc-ωPBEsol	3.854	5.993	1.555	147.4	264.3	148.4	102.5	161.7	88.1
RSHXLDA	3.868	6.119	1.582	134.9	239.6	134.1	90.1	157.2	74.5
HISS	3.864	6.042	1.563	140.1	248.4	141.4	97.1	155.1	77.2
ωB97X	3.895	6.209	1.594	135.4	230.6	136.1	92.5	159.1	72.9
ωB97	3.901	6.231	1.585	133.5	224.1	134.2	89.7	161.4	70.6
HSEsol	3.847	5.955	1.548	143.4	251.5	146.4	101.4	156.2	78.3
HSE06	3.870	6.055	1.565	135.8	237.5	137.4	94.4	151.4	72.1
PBE0	3.869	6.055	1.565	136.1	237.9	137.8	94.4	152.0	72.8
PBEsol0	3.847	5.956	1.548	143.9	252.2	146.8	101.7	157.0	79.1
PBE0-13	3.865	6.044	1.564	138.8	243.4	140.8	96.1	154.8	75.4
B1WC	3.852	5.963	1.548	141.4	245.6	144.2	100.0	155.1	76.5
WC1LYP	3.883	6.108	1.573	134.1	231.3	135.1	92.3	153.6	69.5
B97H	3.896	6.135	1.575	131.1	226.8	124.3	89.8	155.9	72.0
B3PW	3.874	6.078	1.569	133.8	232.9	135.0	92.2	151.2	70.5
PW1PW91	3.871	6.056	1.564	135.7	236.1	137.2	94.3	152.1	71.8
B3LYP	3.897	6.200	1.591	131.7	234.4	135.4	95.2	156.3	74.5
M06L	3.930	5.970	1.519	122.2	221.2	132.4	91.8	116.6	69.3
M06	3.870	6.172	1.595	145.5	237.7	143.0	102.3	173.5	75.9
M06-2x	3.887	6.088	1.566	142.5	243.8	146.1	105.7	150.1	81.1
M06-HF	3.866	5.987	1.548	155.3	274.1	163.4	109.9	165.9	93.7
M05	3.906	6.249	1.600	127.6	220.4	118.9	84.7	155.0	67.4
M05-2x	3.889	6.046	1.555	140.2	246.6	147.7	98.7	149.7	81.6
PBE	3.879	6.059	1.562	108.6	201.3	104.6	74.9	114.8	57.8
HF	3.930	6.256	1.592	131.5	241.7	126.7	86.4	153.5	73.2

Table 3: Cohesive Energies for the primitive cells of CeO₂ and Ce₂O₃

Method	E_{coh} CeO₂(eV)	E_{coh} Ce₂O₃(eV)
Exp (Tabulated)	-20.74 ⁸⁵	-34.99 ⁸⁵
CAM-B3LYP	-19.02	-33.28
Lc-ωBLYP	-18.24	-32.75
Lc-ωPBE	-19.16	-34.00
Lc-ωPBESOL	-19.53	-35.19
RSHXLDA	-19.96	-34.93
HISS	-18.84	-33.29
ωWB97X	-18.96	-33.61
ωB97	-18.64	-33.56
HSESOL	-20.69	-35.12
HSE06	-19.42	-33.37
PBE0	-19.37	-33.36
PBESOL0	-20.64	-35.10
PBE0-13	-19.13	-33.25
B1WC	-20.79	-35.07
WC1LYP	-20.20	-34.18
B97H	-19.29	-33.34
B3PW	-19.18	-32.90
PW1PW1	-18.62	-33.65
B3LYP	-18.76	-32.25
M06L	-20.76	-35.07
M06	-19.20	-33.46
M06-2x	-18.61	-33.90
M06-HF	-20.09	-36.31
M05	-17.73	-31.59
M052x	-18.97	-34.37
PBE	-20.79	-34.39
HF	-25.50	-43.04

Table 4. Vibrational frequencies calculated at the Γ point for CeO_2 and Ce_2O_3 .

Method	CeO_2		Ce_2O_3							
	T_{1u}	T_{2g}	E_g	A_{1g}	E_g	A_{1g}	E_u	A_{2u}	E_u	A_{2u}
Experimental	272 ⁸¹ - 276 ⁸²	465 ^{79,83,84}	103 ⁶⁷	189 ⁶⁷	409 ⁶⁷	409 ⁶⁷	-	-	-	-
CAM-B3LYP	288	465	106	193	424	431	200	214	386	473
LC-ωBLYP	283	460	102	189	421	432	169	209	389	473
Lc-ωPBE	298	472	110	197	432	437	220	230	396	479
Lc-ωPBESOL	314	505	116	207	453	452	235	247	418	494
RSHXLDA	288	468	107	194	427	438	201	218	388	478
HISS	297	474	110	198	433	434	213	228	398	479
ωB97X	249	461	103	193	429	441	201	213	388	475
ωB97	245	446	102	194	419	446	197	218	377	475
HSEsol	304	473	108	205	427	430	211	221	392	462
HSE06	288	461	107	193	423	424	205	218	387	467
PBE0	290	463	107	192	423	425	202	219	388	467
PBEsol0	303	474	112	201	435	432	224	236	399	473
PBE0-13	294	476	108	199	433	450	205	212	399	501
B1WC	301	462	110	198	429	425	221	232	393	466
WC1LYP	285	449	105	191	418	421	212	213	378	461
B97H	164	444	105	195	396	424	202	224	367	478
B3PW	285	454	105	190	418	422	193	214	382	464
PW1PW	288	457	106	192	421	422	204	218	384	464
B3LYP	270	443	100	183	410	418	179	195	372	458
M06L	256	425	109	191	390	423	218	235	373	424
M06	246	446	102	193	412	423	204	197	376	480
M06-2x	324	472	111	195	434	436	236	223	401	484
M06-HF	446	548	119	207	487	433	276	218	444	511
M05	178	431	97	191	384	429	180	216	349	474
M052x	378	499	107	199	469	428	227	212	437	475
PBE	272	424	103	182	399	400	199	205	363	421
HF	280	517	106	191	440	443	201	203	413	479

Table 5: Summary table for the Oxygen vacancies on CeO₂(111). Oxygen vacancy formation energy on surface ($E_{v\text{Surf}}$) and subsurface ($E_{v\text{Sub}}$) positions. With $\mu_{\text{Ce}^{3+}}$ we indicate the magnetic moment over the formally Ce³⁺. \bar{r} (Errore. Il segnalibro non è definito.Errore. Il segnalibro non è definito.Ce³⁺-O) is the average distance between Ce³⁺ and the O in its first coordination shell. R_f is the relaxation factor, computed as the ratio between \bar{r} (Errore. Il segnalibro non è definito.Errore. Il segnalibro non è definito.Ce³⁺-O) and the average Ce-O distance in the pristine surface. $2p - 4f$ is the gap between the valence O $2p$ states and the occupied Ce $4f$ states, while $4f - 4f$ is the gap between the occupied Ce $4f$ states and the conduction empty Ce $4f$ states. The slash divided the data for the two reduced Ce³⁺.

Method	$E_{v\text{Surf}}$ (eV) ^a	$2p - 4f$ (eV)	$4f - 4f$ (eV)	$\mu_{\text{Ce}^{3+}}(\mu_B)$	\bar{r} (Errore. Il segnalibro non è definito.Errore. Il segnalibro non è definito.Ce ³⁺ -O) (Å) ^b	R_f	$E_{v\text{Sub}}$ (eV) ^a	$2p - 4f$ (eV)	$4f - 4f$ (eV)	$\mu_{\text{Ce}^{3+}}(\mu_B)$	\bar{r} Ce ³⁺ -O (Å) ^b	R_f
PBE0(25)/this work	3.00 (3.10)	1.80	1.96	1.000/0.999	2.374/2.371 (2.330)	1.018	2.77 (2.87)	1.99	1.87	1.000/1.000	2.388/2.387 (2.330)	1.025
HSE06(25, screen)/this work	3.10 (3.19)	1.89	1.25	0.997/0.996	2.372/2.371 (2.330)	1.018	2.86 (2.96)	1.99	1.17	1.000/1.000	2.387/2.387 (2.330)	1.024
PW1PW91(20)/this work	3.39 (3.56)	2.02	1.26	0.994/0.995	2.364/2.366 (2.335)	1.013	3.04 (3.20)	2.13	1.02	1.000/1.000	2.385/2.385 (2.335)	1.021
B1WC(16)/this work	3.78 (4.15)	2.40	0.55	0.969/0.969	2.347/2.346 (2.323)	1.010	3.63 (4.00)	2.50	0.22	0.962/0.961	2.362/2.363 (2.323)	1.017
HSE06/p(2x2) 3L ⁵³	3.30		1.0				3.21		0.9			
HSE06/p(4x4) ¹⁴	2.44						2.26					

PBE0/PEECM ⁷⁵	3.3(T) ^c	2.5	3.54(T) ^c /3.33(S) ^c	2.2
--------------------------	---------------------	-----	--	-----

- a) In brackets: the energies calculated with respect to the ground state energy of O (triplet state) and 1/2 of the experimental binding for O₂ (2.58 eV)⁸⁶.
- b) In brackets: the average Ce-O distance for the Ce in the 2th atomic layer of the relaxed pristine surface
- c) T and S are respectively Triplet and Singlet spin multiplicity for the ferromagnetic and antiferromagnetic configuration.

TOC

